

Gapless higher-order topology and corner states in Floquet systems

Longwen Zhou,^{1,2,3,*} Rongtao Wang,¹ and Jiaxin Pan¹

¹*College of Physics and Optoelectronic Engineering,
Ocean University of China, Qingdao, China 266100*

²*Key Laboratory of Optics and Optoelectronics, Qingdao, China 266100*

³*Engineering Research Center of Advanced Marine Physical
Instruments and Equipment of MOE, Qingdao, China 266100*

(Dated: 2025-01-15)

Abstract

Higher-order topological phases (HOTPs) possess localized and symmetry-protected eigenmodes at corners and along hinges in two and three dimensional lattices. The numbers of these topological boundary modes will undergo quantized changes at the critical points between different HOTPs. In this work, we reveal unique higher-order topology induced by time-periodic driving at the critical points of topological phase transitions, which has no equilibrium counterparts and also goes beyond the description of gapped topological matter. Using an alternately coupled Creutz ladder and its Floquet-driven descendants as illustrative examples, we analytically characterize and numerically demonstrate the zero and π corner modes that could emerge at the critical points between different Floquet HOTPs. Moreover, we propose a unified scheme of bulk-corner correspondence for both gapless and gapped Floquet HOTPs protected by chiral symmetry in two dimensions. Our work reveals the possibility of corner modes surviving topological transitions in Floquet systems and initializes the study of higher-order Floquet topology at quantum criticality.

I. INTRODUCTION

Topological phases of matter constitutes one focus of research in condensed matter physics over the past four decades. Renowned discoveries in this area include topological insulators and topological superconductors, whose nontrivial topology are classified by their underlying symmetries and stabilized by the presence of spectral excitation gaps [1–7]. In recent years, the study of topological matter has also been driven towards gapless systems, with the Weyl semimetal be one notable example [8–11]. Generally speaking, a gapless symmetry-protected topological (gSPT) phase does not have an excitation gap between its highest occupied and lowest unoccupied bulk states. Yet, it could possess topological states that are robust to symmetry-preserving perturbations even in the absence of a spectral gap. Compared with topological semimetals, a generic difference of the gSPT phase is that it does not require any forms of gaps in the energy-momentum parameter space to sustain its topological features. Interestingly, it was discovered that the transition points between different topological phases, where the spectral gaps are required to close, can also be classified into topologically trivial and nontrivial ones [12]. The latter holds topological signatures that are usually

* zhoulw13@u.nus.edu

associated with emergent symmetries at critical points, such as degenerate zero modes in the energy and entanglement spectra [13], whose characterizations go beyond the standard paradigms of continuous phase transitions and gapped topological matter [14]. This intriguing phenomenon, sometimes also referred to as topologically nontrivial quantum critical points (QCPs) or symmetry-enriched quantum criticality, has attracted great recent interest in both theoretical and experimental studies [15–56]. Nevertheless, most existing work on topological QCPs are centered on static one-dimensional (1D) systems in thermal equilibrium. The possibility of having symmetry-protected gapless topology beyond equilibrium and 1D setups is much less explored.

Floquet (time-periodic) driving has been shown to be a powerful strategy of pushing a system out-of-equilibrium while generating rich topological phenomena with no static counterparts. For example, a high-frequency driving field may break the time-reversal symmetry and induce the band inversion at a Dirac cone, transforming a trivial semimetal into a topological Chern insulator [57]. A near-resonant and strong driving field may further generate long-range couplings and greatly reshuffle the band structure of a static system, yielding gapped Floquet phases with large topological invariants [58] and many topological edge states [59]. Beyond equilibrium analogs, time-periodic driving can also generate anomalous edge modes with degeneracy at nonzero quasienergies [60] or edge [61] (and even bulk [62]) bands twisting around the whole quasienergy Brillouin zone, which could not be described by the conventional bulk-boundary correspondence of static topological phases. These attractive phenomena have been investigated intensively in the last fifteen years (e.g., see [63–72] for reviews). A key point is that the stroboscopic topological properties of Floquet states are mainly encoded in the Floquet (one-period evolution) operator of the system and its quasienergy (eigenphase) spectrum, making it possible for extending the topological band theory to periodically driven systems. With a bandstructure description, Floquet systems offer a reasonable starting point to explore topologically nontrivial QCPs and gSPT phases beyond equilibrium. Very recently, it was identified that degenerate Majorana zero and π edge modes could emerge at the phase boundaries between different Floquet topological superconductors [73, 74]. Moreover, the topology of these Majorana modes *cannot* be related to standard winding numbers of gapped topological phases in one dimension. They are instead characterized by generalized topological invariants that are tailored to work both away from and exactly at Floquet QCPs [73, 74]. These discoveries initialize the study of

Floquet gSPT phases. Beyond one spatial dimension, rich varieties of symmetry-protected gapless Floquet topology are still awaited to be revealed.

A topological phase of order n in d spatial dimensions holds nontrivial edge states along its $(d - n)$ -dimensional boundaries [75–78]. HOTPs appear in the cases with $d \geq n > 1$ [79–87], whose Floquet counterparts have been explored in a series of recent studies [88–124]. In this work, we uncover and characterize the nontrivial topology and degenerate corner modes at the critical points between distinct Floquet second-order topological phases (SOTPs) in two-dimensional (2D) systems ($n = d = 2$), thereby extending the concept of topologically nontrivial QCPs to Floquet HOTPs. We first introduce a minimal 2D lattice model via a coupled ladder construction [88] in Sec. II. The Hamiltonian of the system possesses a second-order topological insulator (SOTI) phase with zero-energy corner modes and a trivial insulator phase without corner modes. We analytically show that the critical point separating these two phases is *topologically trivial* from the perspectives of bulk topological indices and corner modes. Applying time-periodic quenches to the static coupled-ladder model, we obtain various SOTPs unique to Floquet systems, which are further separated by *topologically nontrivial* critical points. Theoretical and numerical descriptions of the higher-order bulk topology, corner modes and bulk-corner correspondence emerging at these Floquet topological transition points are systematically worked out in Sec. III, which are based on generalized definitions of topological winding numbers and analytical solutions of Floquet corner modes. Considering different driving protocols, we demonstrate in Sec. IV that arbitrarily many zero- and π -quasienergy corner modes could survive together at the critical points between different Floquet SOTPs, providing strong evidence for the presence of nonequilibrium higher-order topology without gap protections. In Sec. V, we summarize our results and discuss potential further studies.

II. STATIC SOTPS WITH TRIVIAL CRITICAL POINTS

In this section, we introduce a typical 2D lattice model that could realize SOTPs through a coupled-ladder construction. We further show that the critical point separating the trivial insulator and SOTI phases of this model is topologically trivial.

We start with a convenient scheme of generating HOTPs in d spatial dimensions, which is proceeded by coupling n -dimensional, lower-order topological states along the extra $(d - n)$

dimensions ($1 \leq n < d$) [88]. As one minimal example following this scheme, let us consider a 2D lattice model described by the Hamiltonian $H = H_x \oplus H_y$. Here, \oplus denotes the Kronecker sum. H_x and H_y represent 1D lattice Hamiltonians along the x and y directions of the $x-y$ plane, respectively. By definition, the Hamiltonian H can be equivalently written as

$$H = H_x \otimes I_y + I_x \otimes H_y, \quad (1)$$

where I_x (I_y) is the identity operator in the Hilbert space of H_x (H_y). Under the open boundary condition (OBC), if H_x has an edge state $|\psi\rangle$ of eigenenergy E around its left boundary, while H_y has an edge state $|\psi'\rangle$ of eigenenergy E' around its lower boundary, we must have a corner state $|\Psi\rangle = |\psi\rangle \otimes |\psi'\rangle$ of eigenenergy $E + E'$ around the lower-left corner of the 2D system described by the H in Eq. (1). Moreover, if $|\psi\rangle$ ($|\psi'\rangle$) possesses a g -(g' -)fold degeneracy protected by some symmetry \mathcal{G} (\mathcal{G}'), the corner state $|\Psi\rangle = |\psi\rangle \otimes |\psi'\rangle$ must be $(g \cdot g')$ -fold degenerate at the energy $E + E'$, which is protected by the composite symmetry $\mathcal{G} \otimes \mathcal{G}'$ [88]. For example, let H_x and H_y be 1D topological insulators with twofold degenerate edge modes at zero energy, which maybe protected by their chiral (sublattice) symmetries \mathcal{S}_x and \mathcal{S}_y . We could then have fourfold degenerate, zero-energy corner modes in the system described by the H in Eq. (1), which are protected by the composite chiral symmetry $\mathcal{S} \equiv \mathcal{S}_x \otimes \mathcal{S}_y$. HOTPs in other spatial dimensions and with different symmetry groups may be generated following the same strategy [88].

In this work, we are mainly interested in the critical points of SOTPs in 2D systems. To be concrete and without loss of generality, we choose the H_x and H_y in Eq. (1) as tight-binding Hamiltonians of the Creutz ladder (CL) model [125] and the Su-Schrieffer-Heeger (SSH) model [126]. The lattice geometries of these models are illustrated in Fig. 1(a). At half-filling, both models constitute prototypes of 1D topological insulators with symmetry-protected edge zero modes. Under periodic boundary conditions (PBCs), their Bloch Hamiltonians in momentum space are given by

$$H_x(k_x) = [J_{x0} + J_{x1} \cos(k_x)]\sigma_x + J_{x1} \sin(k_x)\sigma_z, \quad (2)$$

$$H_y(k_y) = [J_{y0} + J_{y1} \cos(k_y)]\tau_x + J_{y1} \sin(k_y)\tau_y, \quad (3)$$

where $\sigma_{x,y,z}$ and $\tau_{x,y,z}$ are Pauli matrices in their usual representations. We will use σ_0 and

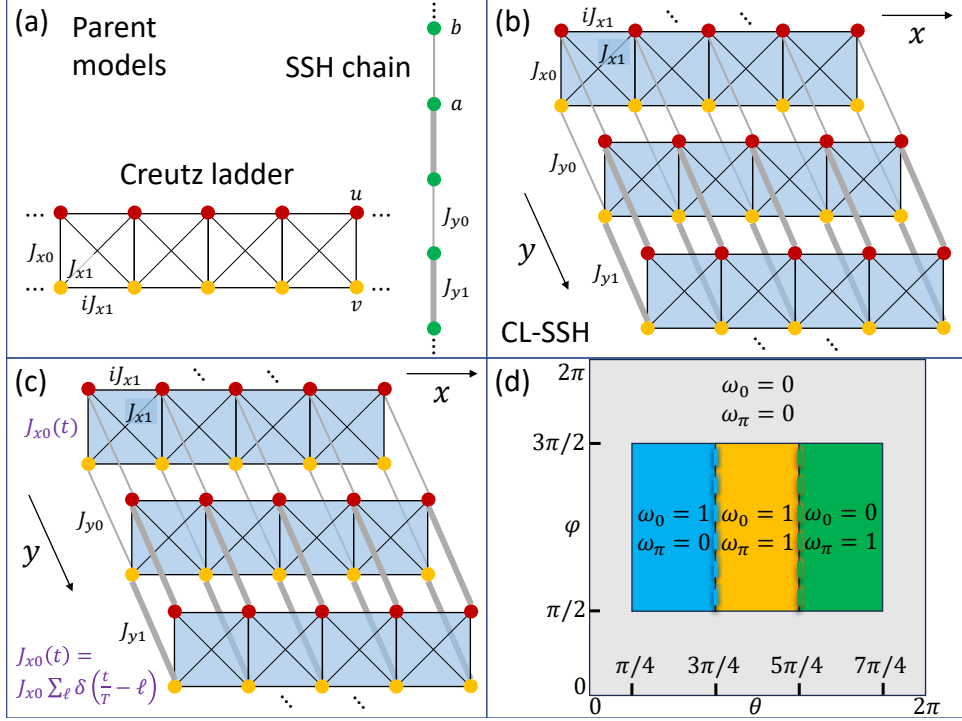


FIG. 1. Schematic diagrams of the lattice models and topological phase diagram of the 2D Floquet system. (a) Geometry of the 1D CL and SSH chain, with system parameters $(J_{x0}, J_{x1}, J_{y0}, J_{y1})$ indexed along the corresponding links. (b) A series of CL, each lies along the x -direction and subject to staggered couplings between adjacent ladders along the y -direction, forming a 2D system that could support SOTPs. (c) CL-SSH coupled model under time-periodic driving, with delta kicks applied to all the inter-leg couplings of each CL, yielding a 2D system that could possess Floquet SOTPs. (d) Floquet topological phase diagram of the periodically kicked CL-SSH model in (c). Each region with a uniform color corresponds to a Floquet SOTI phase, whose topological invariants (ω_0, ω_π) are shown. The blue (green) dashed line denotes a topologically nontrivial phase boundary, characterized by the winding number $\omega_0 = 1$ ($\omega_\pi = 1$) under PBCs and the number of Floquet topological corner modes $N_0 = 4$ ($N_\pi = 4$) at quasienergy 0 (π) under OBCs. Other phase boundaries are topologically trivial. The hopping amplitudes are parameterized as $J_{x0} = \frac{\pi}{2} - \frac{\pi}{4} \sin \theta$, $J_{x1} = \frac{\pi}{2} - \frac{\pi}{4} \cos \theta$, $J_{y0} = \frac{\pi}{2} + \frac{\pi}{4} \cos \varphi$ and $J_{y1} = \frac{\pi}{2} - \frac{\pi}{4} \cos \varphi$ in (d). Ticks along θ - and φ -axes highlight the locations of phase boundaries.

τ_0 to denote 2×2 identity matrices. $k_x \in [-\pi, \pi)$ and $k_y \in [-\pi, \pi)$ are quasimomenta along the x and y directions. In Eq. (2), $J_{x0} \in \mathbb{R}$ denotes the nearest-neighbor (NN) intracell coupling between the two legs of the CL, while the NN intercell coupling along each leg and between the two legs are set to be the same as $J_{x1} \in \mathbb{R}$. There is a π magnetic flux (1/2 flux quantum) through each plaquette of the CL [125]. In Eq. (3), $J_{y0} \in \mathbb{R}$ and $J_{y1} \in \mathbb{R}$ denote the intracell and intercell NN hopping amplitudes along the SSH chain.

The characterization of topological phases in CL and SSH models are well-established (e.g., see Ref. [127] for a review). Here we recap them briefly.

The Hamiltonian $H_x(k_x)$ of the CL possesses the chiral symmetry $\mathcal{S}_x = \sigma_y$, the time-reversal symmetry $\mathcal{T}_x = \sigma_x$ and the particle-hole symmetry $\mathcal{C}_x = \sigma_z$, in the sense that

$$\begin{cases} \mathcal{S}_x H_x(k_x) \mathcal{S}_x = -H_x(k_x), & \mathcal{S}_x^2 = \sigma_0, \\ \mathcal{T}_x H_x^*(k_x) \mathcal{T}_x^\dagger = H_x(-k_x), & \mathcal{T}_x^2 = \sigma_0, \\ \mathcal{C}_x H_x^*(k_x) \mathcal{C}_x^\dagger = -H_x(-k_x), & \mathcal{C}_x^2 = \sigma_0. \end{cases} \quad (4)$$

Therefore, the CL with a π magnetic flux per plaquette belongs to the symmetry class BDI [4]. At half-filling, its gapped topological phases can be characterized by a quantized winding number $w_x \in \mathbb{Z}$, defined as

$$w_x = \int_{-\pi}^{\pi} \frac{dk_x}{2\pi} \frac{\partial \phi_x(k_x)}{\partial k_x}, \quad (5)$$

where $\phi_x(k_x) = \arctan\{J_{x1} \sin(k_x)/[J_{x0} + J_{x1} \cos(k_x)]\}$. w_x counts the number of times that the two-component vector $(J_{x0} + J_{x1} \cos(k_x), J_{x1} \sin(k_x))$ winds around the origin when k_x goes over the first Brillouin zone. It can be inspected from Eqs. (2) and (5) that

$$w_x = \begin{cases} 0, & |J_{x1}| < |J_{x0}|, \\ \pm 1/2, & |J_{x1}| = |J_{x0}|, \\ \pm 1, & |J_{x1}| > |J_{x0}|. \end{cases} \quad (6)$$

Therefore, at half-filling, the CL belongs to a topologically nontrivial (trivial) insulating phase with the winding number $w_x = \pm 1$ ($w_x = 0$). Under the OBC, two degenerate edge modes at zero energy will appear only in the topologically nontrivial phase due to the bulk-boundary correspondence $N_{0x} = 2|w_x|$, where N_{0x} counts the number of edge zero modes. At the critical point $|J_{x1}| = |J_{x0}|$, the system undergoes a topological phase transition accompanied by the bulk-gap closing of $H_x(k_x)$ at zero energy. We obtain a half-integer-quantized w_x at the critical point according to Eq. (5), which could not tell us whether the phase transition point is topologically nontrivial or not [29]. To overcome this issue, we follow the method of Ref. [13] to find an analytic continuation of $H_x(k_x)$ to the complex plane, yielding the mapping function

$$f_x(z) = J_{x0} + J_{x1}z, \quad z \in \mathbb{C}. \quad (7)$$

Inside the unit circle $|z| = 1$, the number of zeros N_{xz} of $f_x(z)$ minus the number of its poles N_{xp} (including their multiplicities and orders) defines a generalized winding number

$$\omega_x \equiv N_{xz} - N_{xp}. \quad (8)$$

For the CL, a direct inspection of Eq. (7) yields

$$\omega_x = \begin{cases} 0, & |J_{x1}| \leq |J_{x0}|, \\ 1, & |J_{x1}| > |J_{x0}|. \end{cases} \quad (9)$$

Therefore, we have $\omega_x = w_x$ in the gapped phases of CL. The critical point $|J_{x1}| = |J_{x0}|$ tends out to be topologically trivial with $\omega_x = 0$, having no degenerate edge modes at zero energy under the OBC. The topological triviality of this critical point can be verified by computing the zero-energy solution of the CL under the OBC. Taking a half-infinite chain with unit-cell indices $m = 1, 2, \dots, \infty$, we find the zero-energy solution of the CL as

$$|\psi_L\rangle = \sum_{m=1}^{\infty} \left(-\frac{J_{x0}}{J_{x1}} \right)^{m-1} (\hat{u}_m^\dagger - i\hat{v}_m^\dagger)|\emptyset\rangle, \quad (10)$$

where ‘‘L’’ means left, \hat{u}_m^\dagger (\hat{v}_m^\dagger) creates a fermion in the sublattice u (v) of the m th unit cell on the upper (lower) leg of the ladder [see Fig. 1(a)], and $|\emptyset\rangle$ denotes the vacuum state. There would be another such edge mode if the OBC is taken at $m = \infty$ (for details, see Appendix A). These degenerate edge modes become extended at $|J_{x1}| = |J_{x0}|$, so that they could not survive at the critical point. We can then propose a refined bulk-edge correspondence for the CL, i.e.,

$$N_{0x} = 2\omega_x = \begin{cases} 0, & |J_{x1}| \leq |J_{x0}|, \\ 2, & |J_{x1}| > |J_{x0}|, \end{cases} \quad (11)$$

which holds true in both gapped phases and along phase boundaries. It confirms that the transition point between the topological and trivial insulator phases of the CL is itself topologically trivial.

The symmetry, topology and bulk-edge correspondence of the SSH model can be treated following the same routine. We first identify the chiral symmetry $\mathcal{S}_y = \tau_z$, time-reversal

symmetry $\mathcal{T}_y = \tau_0$, and particle-hole symmetry $\mathcal{C}_y = \tau_z$ of the $H_y(k_y)$ in Eq. (3), i.e.,

$$\begin{cases} \mathcal{S}_y H_y(k_y) \mathcal{S}_y = -H_y(k_y), & \mathcal{S}_y^2 = \tau_0, \\ \mathcal{T}_y H_y^*(k_y) \mathcal{T}_y^\dagger = H_y(-k_y), & \mathcal{T}_y^2 = \tau_0, \\ \mathcal{C}_y H_y^*(k_y) \mathcal{C}_y^\dagger = -H_y(-k_y), & \mathcal{C}_y^2 = \tau_0. \end{cases} \quad (12)$$

The SSH model thus also belongs to the symmetry class BDI [4]. At half-filling, its gapped topological phases can be characterized by a quantized winding number $w_y \in \mathbb{Z}$, which is defined as

$$w_y = \int_{-\pi}^{\pi} \frac{dk_y}{2\pi} \frac{\partial \phi_y(k_y)}{\partial k_y}, \quad (13)$$

where $\phi(k_y) = \arctan\{J_{y1} \sin(k_y)/[J_{y0} + J_{y1} \cos(k_y)]\}$. w_y counts the number of times that the two-component vector $(J_{y0} + J_{y1} \cos(k_y), J_{y1} \sin(k_y))$ encircles the origin when k_y goes over the first Brillouin zone. It can be deduced from Eqs. (3) and (13) that

$$w_y = \begin{cases} 0, & |J_{y1}| < |J_{y0}|, \\ \pm 1/2, & |J_{y1}| = |J_{y0}|, \\ \pm 1, & |J_{y1}| > |J_{y0}|. \end{cases} \quad (14)$$

The issue is similar to that of the CL. Following the approach of Ref. [13], the complex mapping function of $H_y(k_y)$ should take the form

$$f_y(z) = J_{y0} + J_{y1}z, \quad z \in \mathbb{C}. \quad (15)$$

Counting the zeros N_{yz} and poles N_{yp} of $f_y(z)$ inside the unit circle $|z| < 1$ yields the following generalized winding number for the SSH model, i.e.,

$$\omega_y \equiv N_{yz} - N_{yp} = \begin{cases} 0, & |J_{y1}| \leq |J_{y0}|, \\ 1, & |J_{y1}| > |J_{y0}|. \end{cases} \quad (16)$$

It further predicts the bulk-edge correspondence

$$N_{0y} = 2\omega_y = \begin{cases} 0, & |J_{y1}| \leq |J_{y0}|, \\ 2, & |J_{y1}| > |J_{y0}|, \end{cases} \quad (17)$$

where N_{0y} counts the number of degenerate zero-energy edge modes when the OBC is taken at both edges of the SSH chain. In conclusion, we find that when the intracell (intercell) hopping is stronger, the ground-state of the SSH model at half-filling corresponds to a topologically trivial (nontrivial) insulating phase, which has no (two) degenerate edge modes at zero energy under the OBC. The critical point $|J_{y1}| = |J_{y0}|$ should be topologically trivial too, as it has $\omega_y = 0$ and there are no degenerate edge zero modes ($N_{0y} = 0$) there. This triviality can be verified by computing the zero-energy solutions of the SSH model. Considering a half-infinite chain with unit-cell indices $n = 1, 2, \dots, \infty$, the zero-energy solution of SSH model reads

$$|\psi'_B\rangle = \sum_{n=1}^{\infty} \left(-\frac{J_{y0}}{J_{y1}} \right)^{n-1} \hat{a}_n^\dagger |\emptyset\rangle, \quad (18)$$

where “B” means bottom, \hat{a}_n^\dagger creates a fermion in the sublattice a of the n th unit cell [see Fig. 1(a)], and $|\emptyset\rangle$ denotes the vacuum state. There is one more edge zero mode if the OBC is taken at $n = \infty$ (for details, see Appendix A). These edge modes could not survive at $|J_{y1}| = |J_{y0}|$, where they become extended into the bulk. They can only be exponentially localized when $|J_{y1}| > |J_{y0}|$, i.e., within the topologically nontrivial phase. Therefore, the transition point between the topological and trivial insulator phases of the SSH model is indeed topologically trivial. In parallel with the CL, Eqs. (16) and (17) depict the topology and bulk-edge correspondence of the SSH model throughout its parameter space, including both gapped and gapless phases.

With the CL and SSH models as building blocks, we could straightforwardly construct a “minimal” model holding 2D SOTPs, whose Hamiltonian under the PBC takes the form

$$H(k_x, k_y) = H_x(k_x) \otimes \tau_0 + \sigma_0 \otimes H_y(k_y), \quad (19)$$

where $H_x(k_x)$ and $H_y(k_y)$ are given by the Bloch Hamiltonians of CL and SSH models in

Eqs. (2) and (3), respectively. The lattice geometry of this 2D system is illustrated in Fig. 1(b). As discussed at the beginning of this section, if the 1D CL and SSH parents both possess zero-energy edge modes, their 2D descendant, as defined by Eq. (1) will hold zero-energy eigenstates around the corners of the 2D lattice under the OBCs so long as their protecting symmetries (here the chiral symmetries) are preserved. To be explicit, consider a semi-infinite system with unit-cell indices $(m, n) \in \mathbb{Z}^+ \times \mathbb{Z}^+$, which has an open corner at $(m, n) = (1, 1)$. With Eqs. (10) and (18), we can obtain a zero-energy solution of the 2D system (up to a normalization factor) as

$$|\Psi_{\text{LB}}\rangle \equiv |\psi_{\text{L}}\rangle \otimes |\psi'_{\text{B}}\rangle = \sum_{m,n=1}^{\infty} \left(-\frac{J_{x0}}{J_{x1}}\right)^{m-1} \left(-\frac{J_{y0}}{J_{y1}}\right)^{n-1} (|m, u\rangle - i|m, v\rangle) \otimes |n, a\rangle. \quad (20)$$

This state is exponentially localized around $(m, n) = (1, 1)$ (i.e., a corner zero mode) if and only if $|J_{x1}| > |J_{x0}|$ and $|J_{y1}| > |J_{y0}|$, implying that both the CL and SSH models must be set into their topologically nontrivial gapped regions. Based on Eqs. (8) and (16), a composite winding number ω can be introduced to account this fact, i.e.,

$$\omega \equiv \omega_x \omega_y = \begin{cases} 1, & |J_{x1}| > |J_{x0}| \quad \& \quad |J_{y1}| > |J_{y0}|, \\ 0, & \text{otherwise.} \end{cases} \quad (21)$$

At half-filling, our 2D system then represents an SOTI (a trivial insulator) if $\omega = 1$ ($\omega = 0$). The integer-quantization of ω is preserved so long as the composite chiral symmetry $\mathcal{S} \equiv \mathcal{S}_x \otimes \mathcal{S}_y = \sigma_y \otimes \tau_z$ of $H(k_x, k_y)$ [Eq. (19)], satisfying

$$\mathcal{S}H(k_x, k_y)\mathcal{S} = -H(k_x, k_y), \quad \mathcal{S}^2 = \sigma_0 \otimes \tau_0, \quad (22)$$

remains intact. Regarding the bulk-corner correspondence, if $|\Psi_{\text{LB}}\rangle$ represents a corner zero modes, we will have three other corner zero modes (for details, see Appendix A) under the OBCs along both dimensions. The total number of these corner modes N_0 can thus be associated to the winding number ω as

$$N_0 = 4\omega = \begin{cases} 4, & |J_{x1}| > |J_{x0}| \quad \& \quad |J_{y1}| > |J_{y0}|, \\ 0, & \text{otherwise.} \end{cases} \quad (23)$$

Model	Topological phase boundary	Topological invariant	Bulk-boundary correspondence
CL	$ J_{x1} = J_{x0} $	$\omega_x = \begin{cases} 0, & J_{x1} \leq J_{x0} \\ 1, & J_{x1} > J_{x0} \end{cases}$	$N_{0x} = 2\omega_x$
SSH	$ J_{y1} = J_{y0} $	$\omega_y = \begin{cases} 0, & J_{y1} \leq J_{y0} \\ 1, & J_{y1} > J_{y0} \end{cases}$	$N_{0y} = 2\omega_y$
Coupled CL-SSH	$ J_{x1} = J_{x0} $ or $ J_{y1} = J_{y0} $	$\omega = \begin{cases} 0, & J_{x1} \leq J_{x0} \text{ or } J_{y1} \leq J_{y0} \\ 1, & J_{x1} > J_{x0} \text{ \& } J_{y1} > J_{y0} \end{cases}$	$N_0 = 4\omega$

TABLE I. Summary of the results for the CL, SSH and coupled CL-SSH models regarding their bulk topological phases, topological phase boundaries (critical points) and bulk-boundary (-edge or -corner) correspondence. Meanings of the system parameters are given in the paragraph below Eqs. (2) and (3). Definitions of the winding numbers are given in Eqs. (8), (16) and (21). N_{0x} and N_{0y} are the numbers of degenerate edge modes of the CL and SSH models at zero energy, respectively. N_0 is the number of degenerate corner modes of the coupled CL-SSH model at zero energy under OBCs.

Notably, all the corner modes disappear in the critical parameter space $|J_{x1}| = |J_{x0}|$ with any (J_{y0}, J_{y1}) , or $|J_{y1}| = |J_{y0}|$ with any (J_{x0}, J_{x1}) . The topological phase boundaries of our 2D CL-SSH coupled model are thus topologically trivial, characterized by the vanishing of generalized winding number ω and the delocalization of corner zero mode $|\Psi_{\text{LB}}\rangle$ in Eq. (20).

In Table I, we summarize the main results regarding the topology and bulk-boundary correspondence of the CL, SSH and coupled CL-SSH models in this section. The key point is that at the critical points between the topological and trivial gapped phases of these models, symmetry-protected degenerate edge or corner zero modes are *absent*. In this sense, the phase boundaries between distinct insulating phases in these static systems are topologically trivial. In the next section, we will show that under Floquet driving, the original critical points of our static 2D system could become topologically nontrivial, carrying fourfold-degenerate Floquet eigenmodes with zero and π quasienergies at the corners. These higher-order topological states can coexist with a gapless quasienergy bulk, making them unique to Floquet critical systems. Moreover, new phase boundaries holding topological corner modes can be generated by Floquet driving, which have no counterparts in the static setup.

III. FLOQUET SOTPS WITH TOPOLOGICALLY NONTRIVIAL CRITICAL POINTS

We now apply Floquet driving to the 2D lattice model introduced in the last section. To emphasize the main physics, we focus on a simple driving protocol, in which the intracell

coupling between the two legs of each CL is subject to a string of equally paced delta pulses [see Fig. 1(c) for an illustration]. The time-dependent Bloch Hamiltonian of such a delta kicked CL-SSH model is given by

$$H(k_x, k_y, t) = H_x(k_x, t) \otimes \tau_0 + \sigma_0 \otimes H_y(k_y), \quad (24)$$

where $H_y(k_y)$ is the Hamiltonian of the SSH model in Eq. (3), and

$$H_x(k_x, t) = H_{x0}\delta_T(t) + H_{x1}(k_x), \quad (25)$$

$$H_{x0} = J_{x0}\sigma_x, \quad (26)$$

$$H_{x1}(k_x) = J_{x1}[\cos(k_x)\sigma_x + \sin(k_x)\sigma_z], \quad (27)$$

and $\delta_T(t) \equiv \sum_{\ell \in \mathbb{Z}} \delta(t/T - \ell)$. The NN inter-leg couplings are thus only turned on in a narrow time window at the intersection of each two adjacent driving periods ℓT and $(\ell + 1)T$. The Floquet operator of the system in (k_x, k_y) -space, defined by its evolution operator $U(k_x, k_y) = \hat{\mathbb{T}} e^{-\frac{i}{\hbar} \int_0^T H(k_x, k_y, t) dt}$ over a complete driving period T reads

$$U(k_x, k_y) = e^{-iH_{x0}} e^{-iH_{x1}(k_x)} \otimes e^{-iH_y(k_y)}, \quad (28)$$

where we have set $\hbar/T = 1$ as the unit of energy and $\hat{\mathbb{T}}$ performs the time-ordering. The Floquet operator $U(k_x, k_y)$ has a direct product structure, which allows us to analyze it by considering its 1D parent systems

$$U_x(k_x) \equiv e^{-iH_{x0}} e^{-iH_{x1}(k_x)}, \quad (29)$$

$$U_y(k_y) \equiv e^{-iH_y(k_y)}. \quad (30)$$

First, we notice that the effective Hamiltonian of $U_y(k_y)$, defined formally as $i \ln U_y(k_y)$, is just the static Hamiltonian $H_y(k_y)$ of the SSH model [Eq. (3)] mod 2π , whose symmetry, topology and bulk-edge correspondence have been analyzed in the last section. The quasienergy spectrum of $U_y(k_y)$ is simply given by $\pm \varepsilon'(k_y) \bmod 2\pi$, with $\varepsilon'(k_y) = \sqrt{[J_{y0} + J_{y1} \cos(k_y)]^2 + [J_{y1} \sin(k_y)]^2}$. At half-filling, the gapped topological phases of $U_y(k_y)$ are also characterized by the winding number w_y in Eq. (13). The bulk-edge correspondence throughout its parameter space

(including both gapped and gapless regions) can be further captured by the generalized invariant ω_y in Eq. (16).

The Floquet-induced nontrivial topology of $U(k_x, k_y)$ should then be controlled mainly by its parent $U_x(k_x)$, which describes a periodically kicked CL [128]. The quasienergy spectrum of $U_x(k_x)$ can be obtained by solving its eigenvalue equation $U_x(k_x)|\psi\rangle = e^{-i\varepsilon(k_x)}|\psi\rangle$, yielding the Floquet bands $\pm\varepsilon(k_x) \bmod 2\pi$ with

$$\varepsilon(k_x) = \arccos(\cos J_{x0} \cos J_{x1} - \sin J_{x0} \sin J_{x1} \cos k_x). \quad (31)$$

The bands $\pm\varepsilon(k_x)$ could touch with each other at either the center ($\varepsilon = 0$) or the boundary ($\varepsilon = \pi$) of the first quasienergy Brillouin zone $\varepsilon \in [-\pi, \pi]$. In the parameter space (J_{x0}, J_{x1}) , this allows us to determine the gap-closing condition between $\pm\varepsilon(k_x)$, i.e.,

$$J_{x0} \pm J_{x1} = \nu\pi, \quad \nu \in \mathbb{Z}. \quad (32)$$

In Eq. (32), we take the $+$ ($-$) sign if the critical quasimomentum of gap-closing point appears at $k_x = 0$ ($k_x = \pi$). The two bands meet at the quasienergy $\varepsilon = 0$ ($\varepsilon = \pi$) when ν takes even (odd) integers. In comparison, the static CL [Eq. (2)] only allows $\nu = 0$ (so that $|J_{x1}| = |J_{x0}|$) in order for the system to be critical (gapless). We conclude that the addition of a simple Floquet driving may indeed enrich the phase structure of the static CL greatly. This enrichment can be further carried over to the 2D composite system $U(k_x, k_y) = U_x(k_x) \otimes U_y(k_y)$ following Eq. (28), as will be revealed shortly.

The $U_x(k_x)$ in Eq. (29) does not show any explicit symmetries like the Hamiltonian of the static CL in Eq. (2). To figure out the symmetry-protected topological properties of $U_x(k_x)$, we introduce unitary transformations to a pair of symmetric time frames [129], in which the $U_x(k_x)$ reads

$$U_{1x}(k_x) = e^{-\frac{i}{2}H_{x1}(k_x)} e^{-iH_{x0}} e^{-\frac{i}{2}H_{x1}(k_x)}, \quad (33)$$

$$U_{2x}(k_x) = e^{-\frac{i}{2}H_{x0}} e^{-H_{x1}(k_x)} e^{-\frac{i}{2}H_{x0}}. \quad (34)$$

The $U_{\alpha x}(k_x)$ ($\alpha = 1, 2$) and $U_x(k_x)$ are unitary equivalent, implying that they have the same quasienergy spectrum. Meanwhile, $U_{\alpha x}(k_x)$ has the chiral, time-reversal and particle-hole

symmetries $\mathcal{S}_x = \sigma_y$, $\mathcal{T}_x = \sigma_x$ and $\mathcal{C}_x = \sigma_z$, in the sense that

$$\begin{cases} \mathcal{S}_x U_{\alpha x}(k_x) \mathcal{S}_x = U_{\alpha x}^\dagger(k_x), & \mathcal{S}_x^2 = \sigma_0, \\ \mathcal{T}_x U_{\alpha x}^*(k_x) \mathcal{T}_x^\dagger = U_{\alpha x}^\dagger(-k_x), & \mathcal{T}_x^2 = \sigma_0, \\ \mathcal{C}_x U_{\alpha x}^*(k_x) \mathcal{C}_x^\dagger = U_{\alpha x}(-k_x), & \mathcal{C}_x^2 = \sigma_0, \end{cases} \quad (35)$$

where $\alpha = 1, 2$. Therefore, as the static CL, the system described by $U_x(k_x)$ also belongs to the symmetry class BDI. Its gapped topological phases can then be characterized by a pair of integer quantized winding numbers (w_0, w_π) [129]. To define these topological invariants, we first obtain the winding number of the effective Hamiltonian of $U_{\alpha x}(k_x)$ as

$$w_{\alpha x} = \int_{-\pi}^{\pi} \frac{dk_x}{2\pi} \frac{\partial \phi_{\alpha x}(k_x)}{\partial k_x}, \quad (36)$$

where $\phi_{\alpha x}(k_x) \equiv \arctan(d_{z\alpha}/d_{x\alpha})$, $d_{x\alpha} = \frac{i}{2} \text{Tr}[\sigma_x U_{\alpha x}(k_x)]$ and $d_{z\alpha} = \frac{i}{2} \text{Tr}[\sigma_z U_{\alpha x}(k_x)]$ for $\alpha = 1, 2$. Combining the winding numbers (w_{1x}, w_{2x}) in two time frames allows us to define topological invariants for the kicked CL [Eq. (29)] as

$$(w_{0x}, w_{\pi x}) = \frac{1}{2}(w_{1x} + w_{2x}, w_{1x} - w_{2x}). \quad (37)$$

For 1D Floquet systems in the BDI symmetry class, it has been shown that the winding numbers $(w_{0x}, w_{\pi x})$, as defined in Eq. (37), could fully characterize the topological properties and bulk-edge correspondences of their gapped phases at half-filling [129]. Specially, if N_{0x} and $N_{\pi x}$ denote the numbers of degenerate edge modes at zero and π quasienergies, we would have

$$(N_{0x}, N_{\pi x}) = 2(|w_{0x}|, |w_{\pi x}|). \quad (38)$$

This relation holds true in all the gapped phases of the kicked CL.

Along the critical lines [Eq. (32)], the winding numbers (w_{1x}, w_{2x}) may take either integer or half-integer values, making the bulk-edge correspondence in Eq. (38) inapplicable. We can resolve this issue by generalizing the definition of winding numbers in accordance with Eq. (8) and computing the edge-state solutions analytically at the critical points of the kicked CL. In short, we introduce a pair of generalized winding numbers $(\omega_{x1}, \omega_{x2})$ for $U_{1x}(k_x)$ and $U_{2x}(k_x)$ (for details, see Appendix B). Their linear combinations yield the new topological

invariants

$$(\omega_{x0}, \omega_{x\pi}) = \frac{1}{2}(\omega_{x1} + \omega_{x2}, \omega_{x1} - \omega_{x2}). \quad (39)$$

These invariants are both integer-quantized, and they are applicable in both the gapped phases and at the critical points of the kicked CL (or any other 1D chiral-symmetric driven systems with two bands). In terms of these generalized invariants, the bulk-edge correspondence can be re-established throughout the phase diagram (see Fig. 6 in Appendix B) of the system as

$$(N_{0x}, N_{\pi x}) = 2(|\omega_{0x}|, |\omega_{\pi x}|). \quad (40)$$

This relation is confirmed by the exact solutions Floquet edge modes at quasienergies zero and π in both gapped phases and along topological phase boundaries of the kicked CL (for details, see Appendix B).

We are now ready to unveil the Floquet-induced higher-order topology in the gapped and gapless phases of our 2D system $U(k_x, k_y)$. Starting with Eq. (28) and incorporating the transformations in Eqs. (33) and (33), we arrive at the Floquet operators of our kicked CL-SSH coupled model in two symmetric time frames $\alpha = 1, 2$, i.e.,

$$U_\alpha(k_x, k_y) = U_{\alpha x}(k_x) \otimes e^{-iH_y(k_y)}. \quad (41)$$

From Eqs. (12) and (35), we can straightforwardly identify the chiral, time-reversal and particle-hole symmetries of $U_\alpha(k_x, k_y)$, i.e., $\mathcal{S} = \sigma_y \otimes \tau_z$, $\mathcal{T} = \sigma_x \otimes \tau_0$ and $\mathcal{C} = \sigma_z \otimes \tau_z$. Under their operations, the $U_\alpha(k_x, k_y)$ ($\alpha = 1, 2$) transforms as

$$\begin{cases} \mathcal{S}U_\alpha(k_x, k_y)\mathcal{S} = U_\alpha^\dagger(k_x, k_y), \\ \mathcal{T}U_\alpha^*(k_x, k_y)\mathcal{T}^\dagger = U_\alpha^\dagger(-k_x, -k_y), \\ \mathcal{C}U_\alpha^*(k_x, k_y)\mathcal{C}^\dagger = U_\alpha(-k_x, -k_y), \end{cases} \quad (42)$$

where $\mathcal{S}^2 = \mathcal{T}^2 = \mathcal{C}^2 = 1$. Our kicked CL-SSH model thus also belongs to the symmetry class BDI, whose first-order Floquet topological phases are all trivial in two dimensions. Nevertheless, the 2D driven system described by Eq. (28) could possess Floquet SOTPs. To characterize their topology and bulk-corner correspondence, we propose the definition of

Model	Kicked CL-SSH						
Topological phase boundary	$J_{x0} \pm J_{x1} = \nu\pi, \quad \nu \in \mathbb{Z}$ or $ J_{y1} = J_{y0} $						
Topological invariants $(\omega_0, \omega_\pi) =$	$(1, 1), J_{y1} > J_{y0} $	&	$\tan \frac{J_{x1}}{2} > \tan \frac{J_{x0}}{2}$	&	$\tan \frac{J_{x0}}{2} \tan \frac{J_{x1}}{2} > 1$		
	$(1, 0), J_{y1} > J_{y0} $	&	$\tan \frac{J_{x1}}{2} > \tan \frac{J_{x0}}{2}$	&	$\tan \frac{J_{x0}}{2} \tan \frac{J_{x1}}{2} \leq 1$		
	$(0, 1), J_{y1} > J_{y0} $	&	$\tan \frac{J_{x1}}{2} \leq \tan \frac{J_{x0}}{2}$	&	$\tan \frac{J_{x0}}{2} \tan \frac{J_{x1}}{2} > 1$		
	$(0, 0),$ otherwise						
Bulk-corner correspondence	$(N_0, N_\pi) = 4(\omega_0, \omega_\pi)$						

TABLE II. Summary of the key results for the kicked CL-SSH model concerning its Floquet SOTPs, phase boundaries (i.e., critical points), and bulk-corner correspondence. Definition of the winding numbers are given in Eq. (43). N_0 and N_π are the numbers of degenerate corner modes at zero and π quasienergies under OBCs, respectively.

generalized winding numbers (ω_0, ω_π) as

$$(\omega_0, \omega_\pi) \equiv (|\omega_{0x}\omega_{y}|, |\omega_{\pi x}\omega_{y}|). \quad (43)$$

Here, $(\omega_{0x}, \omega_{\pi x})$ are topological invariants of the kicked CL in Eq. (39), which can also topologically characterize other 1D, two-band chiral-symmetric driven systems. The ω_y , as defined in Eq. (16), is just the generalized winding number of SSH model. Using these bulk topological invariants, we can further count the numbers of Floquet zero and π corner modes N_0 and N_π under the OBCs through the relation

$$(N_0, N_\pi) = 4(\omega_0, \omega_\pi). \quad (44)$$

As a main result of this study, the rule of bulk-corner correspondence in Eq. (44) not only works in all the gapped phases of our kicked CL-SSH model, but also holds along its topological phase boundaries, where at least one spectral gap of $U(k_x, k_y)$ at the quasienergies zero and π closes. Eq. (44) thus captures the gapped and gapless higher-order topology of our kicked CL-SSH model from both the bulk and corner perspectives. In Appendices C and D, we justify the Eq. (44) for our system by evaluating both the (N_0, N_π) and (ω_0, ω_π) analytically, with the key results summarized in Table II. We emphasize that the validity of Eq. (44) is not restricted to our kicked CL-SSH setup. This correspondence is satisfied by any 2D, chiral-symmetric Floquet system whose Hamiltonian shares the form of Eq. (24), in which the driving field is only coupled to degrees of freedom along one spatial dimension.

The topological phase diagram of our kicked CL-SSH model is reported in Fig. 1(d). In parameter regions where the spectra of $U(k_x, k_y)$ are gapped at both zero and π quasienergies, we find one trivial insulator phase with $(\omega_0, \omega_\pi) = (0, 0)$ and three other Floquet SOTI phases. While the SOTI phase with $(\omega_0, \omega_\pi) = (1, 0)$ can appear in static systems, the phases with $(\omega_0, \omega_\pi) = (0, 1)$ and $(\omega_0, \omega_\pi) = (1, 1)$ are new and unique to Floquet settings, with each of them carrying four degenerate corner modes at the quasienergy π under OBCs. Besides, the phase with $(\omega_0, \omega_\pi) = (1, 1)$ possesses four other Floquet corner modes at quasienergy zero. Importantly, we identify two topologically nontrivial phase boundaries, as highlighted by the vertical dashed lines in Fig. 1(d), whose topological properties are endowed uniquely by Floquet driving fields. Along the critical line with $\varphi \in (\pi/2, 3\pi/2)$ at $\theta = 3\pi/4$ in Fig. 1(d), we have four Floquet corner modes at zero quasienergy, which are coexistent with a bulk spectrum that is gapless at quasienergy π . The number of these corner modes is counted by the topological invariants $(\omega_0, \omega_\pi) = (1, 0)$ according to Eq. (44). Along the critical line with $\varphi \in (\pi/2, 3\pi/2)$ at $\theta = 5\pi/4$ in Fig. 1(d), we have four Floquet corner modes at π quasienergy, which are coexistent with a bulk spectrum that is gapless at quasienergy zero. These corner π modes are unique to Floquet systems and their number is counted by the topological invariant $\omega_\pi = 1$ due to Eq. (44). Notably, all the topologically nontrivial phase boundaries will vanish when the driving field is switched off. They are thus of Floquet-origin and represent (together with their associated corner modes) what we do mean by gapless higher-order topology in Floquet systems.

In the rest of this section, we present numerical results to support our theoretical findings. We first consider the Floquet spectra of kicked CL-SSH model under different boundary conditions, which are computed along topological phase boundaries and presented in Fig. 2. The quasienergy spectrum can be obtained by first taking the Fourier transformation of the Floquet operator in Eq. (28) from momentum to position representations, and then solving the eigenvalue equation $U|\Psi\rangle = e^{-i\mathcal{E}}|\Psi\rangle$ under given boundary conditions. In our calculation, we take the unit of energy as the ratio between Planck constant \hbar and driving period T , i.e., $\hbar/T = 1$. The \mathcal{E} is then defined mod 2π and its first quasienergy Brillouin zone is $[-\pi, \pi]$. The Floquet eigenstate can be expanded in position representation $\{|n_x, n_y\rangle\}$ as $|\Psi\rangle = \sum_{n_x=1}^{L_x} \sum_{n_y=1}^{L_y} \Psi_{n_x, n_y} |n_x, n_y\rangle$, where L_x and L_y denote the number of lattice sites along x and y directions. The probability distribution of $|\Psi\rangle$ in lattice space is given by $|\Psi_{n_x, n_y}|^2$ at different sites (n_x, n_y) . The inverse participation ratio (IPR) of $|\Psi\rangle$ is defined

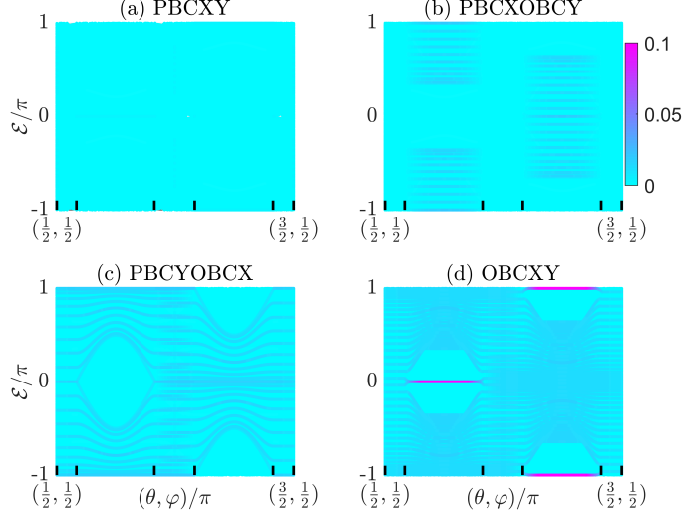


FIG. 2. Quasienergy spectra \mathcal{E} of the kicked CL-SSH model evaluated along topological phase boundaries. The boundary conditions of the system are (a) PBCs along both x and y directions, (b) PBC along x and OBC along y directions, (c) PBC along y and OBC along x directions, and (d) OBCs along both x and y directions. The variables (θ, φ) and related system parameters $(J_{x0}, J_{x1}, J_{y0}, J_{y1})$ are defined following Fig. 1(d). The ticks along the horizontal axis of each panel denote $(\theta, \varphi) = (\pi/2, \pi/2), (3\pi/4, \pi/2), (3\pi/4, 3\pi/2), (5\pi/4, 3\pi/2), (5\pi/4, \pi/2)$ and $(3\pi/2, \pi/2)$ from left to right. Adjacent ticks are connected by straight lines in the (θ, φ) -space of Fig. 1(d), yielding a trajectory along the boundaries between different Floquet phases. The color of each data point represents the IPR of the related eigenstate, whose value is given by the shared color bar of (a)–(d).

as $\text{IPR} = \sum_{n_x, n_y} |\Psi_{n_x, n_y}|^4$, which goes to zero (remains finite) in the limits $L_x \rightarrow \infty$ and $L_y \rightarrow \infty$ if $|\Psi\rangle$ represents an extended (a localized) state.

In Figs. 2(a)–2(d), we find that under any boundary conditions, there are no observable quasienergy gaps in $\mathcal{E} \in [-\pi, \pi]$ throughout the considered parameter space along topological phase boundaries. This is expected, as the quasienergy bands should meet with each other when the system parameters are tuned to the critical points between different Floquet topological phases. Remarkably, we find exponentially localized eigenmodes only when the OBCs are taken along both x and y directions of the lattice, as shown in Fig. 2(d). These modes appear at either the quasienergy zero or π , with their numbers $N_0 = 4$ or $N_\pi = 4$ predicted exactly by the bulk-corner correspondence in Eq. (44) and the solutions of Floquet corner modes in Appendix C. Moreover, they only appear in parameter domains with $(\omega_0, \omega_\pi) = (1, 0)$ and $(\omega_0, \omega_\pi) = (0, 1)$ in Table II. We have thus verified that corner-localized zero and π eigenmodes, as defining features of Floquet SOTPs, could indeed appear at phase boundaries and resist topological phase transitions, forming gapless

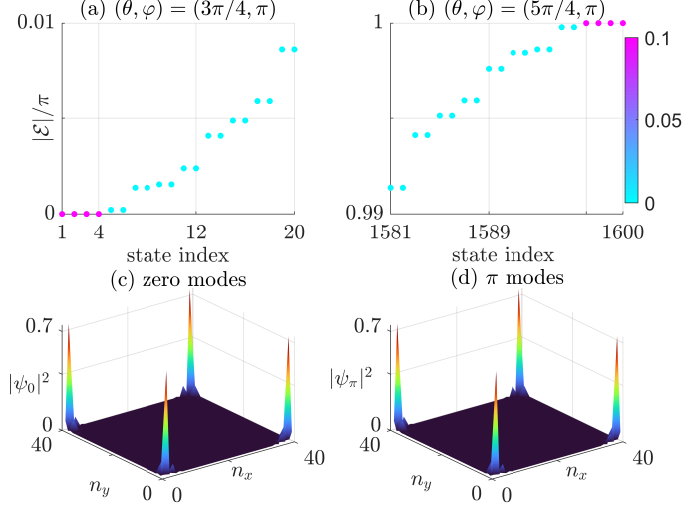


FIG. 3. Floquet corner modes of the kicked CL-SSH model and their probability distributions under OBCs. The variables (θ, φ) and related system parameters $(J_{x0}, J_{x1}, J_{y0}, J_{y1})$ are defined following those of Fig. 1(d). (a) shows the spectrum of the first twenty eigenstates whose quasienergies are closest to $|\mathcal{E}| = 0$ at $(\theta, \varphi) = (3\pi/4, \pi)$. (b) shows the spectrum of the first twenty eigenstates whose quasienergies are closest to $|\mathcal{E}| = \pi$ at $(\theta, \varphi) = (5\pi/4, \pi)$. (a) and (b) share the same color bar, which gives the IPR of each state. (c) shows the probability distributions $|\psi_0|^2$ of the for eigenstates with $|\mathcal{E}| = 0$ in (a). (d) shows the probability distributions $|\psi_\pi|^2$ of the for eigenstates with $|\mathcal{E}| = \pi$ in (b). In (c) and (d), n_x and n_y denote lattice indices along x and y directions.

higher-order topological states at critical points. Specially, the gapless higher-order topology associated to degenerate π corner modes represents a nonequilibrium criticality unique to Floquet-driven systems. Referring to Fig. 1(d), we realize that a topologically nontrivial phase boundary (critical points with corner modes) could only be sandwiched between *topologically distinct and nontrivial* gapped phases. This explains why we find no signatures of corner modes and higher-order topology at any critical points in the non-driven CL-SSH model [Eq. (19)], as the phase boundaries there are all between higher-order *topological and trivial* phases. Besides, we notice in Fig. 2(d) that with the change of system parameters along topological phase boundaries, transitions between gapless Floquet SOTPs (with zero or π corner modes) and gapless trivial phases (without corner modes) could happen. These transitions can be regarded as “*topological phase transitions of topological phase transitions*”, which are also characterized by the topological invariants (ω_0, ω_π) in Eq. (43) and the bulk-corner correspondence in Eq. (44). We conclude that the numerical results in Fig. 2 are all consistent with our theoretical predictions (as summarized in Table II).

To further demonstrate the Floquet corner modes at topological critical points, we present

in Fig. 3 the quasienergies and probability distributions of these corner modes under OBCs. In Figs. 3(a) and 3(b), we find that there are indeed four degenerate eigenmodes at $\mathcal{E} = 0$ ($\mathcal{E} = \pi$) in the quasienergy spectrum when the system parameters are taken at one representative point along the left (right) dashed line of Fig. 1(d). Moreover, only the modes at zero and π quasienergies are strongly localized in space, as highlighted by their IPRs. In Figs. 3(c) and 3(d), we observe that the zero and π eigenmodes are all exponentially localized around the four corners of the lattice, respectively, forming Floquet topological corner modes coexisting with a gapless quasienergy bulk. The emergence of these modes at system corners provide explicit experimental signatures for detecting gapless higher-order topology and phase transitions along higher-order topological phase boundaries in Floquet-driven systems. The numbers of Floquet zero and π corner modes in Figs. 3(c) and 3(d) are coincident with the prediction of invariants (ω_0, ω_π) according to Eq. (44), verifying again the Floquet bulk-corner correspondence.

In conclusion, we have shown that Floquet driving could transform the trivial critical points or gapped phases of static CL-SSH model into topologically nontrivial critical lines (phase boundaries), carrying degenerate corner modes at zero or π quasienergies that are protected by chiral symmetry and coexisted with gapless bulk states. We characterized such second-order topology by a pair of generalized winding numbers (ω_0, ω_π) and established their relationship with the numbers of zero and π corner modes, which work equally well for both gapped and gapless Floquet SOTPs. One remaining question is whether we could have zero and π corner modes to survive together along a topological phase boundary. We give affirmative answer to this question by treating our CL-SSH model under a different driving protocol in the following section.

IV. TOPOLOGICAL PHASE BOUNDARIES WITH COEXISTING ZERO AND π FLOQUET CORNER MODES

In this section, we deal with the possibility of having both zero and π corner modes at the same critical point of Floquet HOTPs. This is not achievable following the driving protocol of Eqs. (24)–(28). The key issue is that there are no Floquet phases whose topological invariants ω_0 and ω_π are both larger than one in the periodically kicked CL-SSH model we studied. To address this issue, we apply a different driving protocol to each CL in the

CL-SSH model of Fig. 1(b), i.e., we take

$$H'_x(k_x, t) = [J_{x0} + J_{x1} \cos(k_x)]\sigma_x + J'_{x1} \sin(k_x)\delta_T(t)\sigma_z. \quad (45)$$

Compared with the time-periodic Hamiltonian in Eq. (25), there are two differences. First, the periodic kicks $\delta_T(t) \equiv \sum_{\ell \in \mathbb{Z}} \delta(t/T - \ell)$ are now applied to the horizontal NN couplings along each leg of the CL. Second, the intra-leg NN coupling J'_{x1} and inter-leg second-neighbor coupling J_{x1} are now allowed to take different values. These two changes are enough for us to obtain greatly enriched Floquet SOTPs in the resulting 2D system

$$H'(k_x, k_y, t) = H'_x(k_x, t) \otimes \tau_0 + \sigma_0 \otimes H_y(k_y), \quad (46)$$

where $H_y(k_y)$ is still given by Eq. (3) of the SSH model.

Solving the Floquet eigenvalue equation related to $H'_x(k_x, t)$, we obtain its quasienergy dispersion $\varepsilon(k_x) = \arccos[\cos(J_{x0} + J_{x1} \cos k_x) \cos(J'_{x1} \sin k_x)]$. Setting $\varepsilon(k_x) = 0$ or π , we find that the quasienergy gap between Floquet bands $\pm\varepsilon(k_x)$ vanishes when the system parameters satisfy the equation

$$\frac{(\mu\pi - J_{x0})^2}{J_{x1}^2} + \frac{\nu^2\pi^2}{(J'_{x1})^2} = 1, \quad (47)$$

where $\mu, \nu \in \mathbb{Z}$. Specially, the gap closes at quasienergy zero (π) if μ and ν have the same parity (opposite parities). It is clear that this phase-boundary equation is more complicated than Eq. (32), allowing the Floquet operator of the coupled-ladder Hamiltonian $H'(k_x, k_y, t)$ to yields much richer SOTPs in comparison with the kicked CL-SSH model of the last section. The underlying physical reason is that the driving scheme applied in Eq. (45) could induce long-range couplings in the resulting Floquet system, making it possible for the 2D coupled-ladder to have larger-than-one topological invariants.

By definition, the Floquet operator of the system described by Eq. (46) takes the form

$$U'(k_x, k_y) = e^{-i[J_{x0} + J_{x1} \cos(k_x)]\sigma_x} e^{-iJ'_{x1} \sin(k_x)\sigma_z} \otimes e^{-iH_y(k_y)}, \quad (48)$$

where we have taken $\hbar/T = 1$ and considered the evolution period from $t = 0^-$ to $t = T + 0^-$. In symmetric time frames, the $U'(k_x, k_y)$ in Eq. (48) has the same chiral symmetry as the

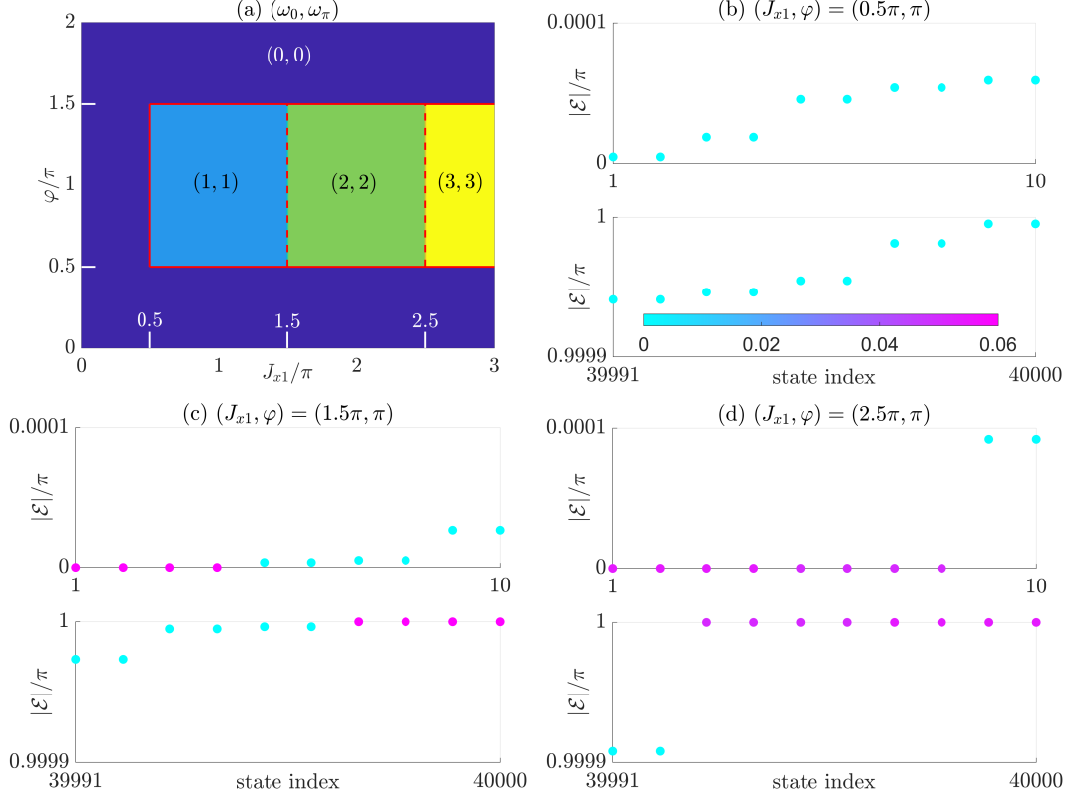


FIG. 4. Topological phase diagram of $U'(k_x, k_y)$ [Eq. (48)] under PBCs [in (a)] and quasienergy spectra of $U'(k_x, k_y)$ around $\mathcal{E} = 0, \pi$ under OBCs [in (b)–(d)]. Other system parameters are $J_{x0} = J'_{x1} = 0.5\pi$, $J_{y0} = \frac{\pi}{2} + \frac{\pi}{4} \cos \varphi$ and $J_{y1} = \frac{\pi}{2} - \frac{\pi}{4} \cos \varphi$ for all panels. (b)–(d) share the same color bar, encoding the IPR of each eigenstate. The lattice size is set to $L_x = L_y = 200$ for (b)–(d).

$U(k_x, k_y)$ in Eq. (28). Their Floquet SOTPs and bulk-corner correspondence can thus be characterized by the same theoretical framework according to Eqs. (43) and (44). In Fig. 4, we obtain the topological phase diagram of $U'(k_x, k_y)$ under PBCs and present the Floquet spectra of $U'(k_x, k_y)$ around the center ($\mathcal{E} = 0$) and boundary ($\mathcal{E} = \pi$) of the first quasienergy Brillouin $\mathcal{E} \in [-\pi, \pi]$ under the OBCs. In Fig. 4(a), we observe one trivial insulating phase and three Floquet SOTI phases, characterized by the winding numbers $(\omega_0, \omega_\pi) = (0, 0)$, $(1, 1)$, $(2, 2)$ and $(3, 3)$ in each uniformly colored region. Notably, these phases are separated by two distinct types of phase boundaries. The critical line between trivial and Floquet SOTI phases, highlighted by the red solid line in Fig. 4(a) is itself topologically trivial, featuring no zero or π Floquet corner modes as exemplified in Fig. 4(b) under OBCs. The two critical lines between nontrivial Floquet SOTI phases, emphasized by the red dashed lines in Fig. 4(a) are yet topologically nontrivial, carrying fourfold-degenerate Floquet corner modes at both zero and π quasienergies as showcased in Figs. 4(c) and 4(d) under OBCs. There

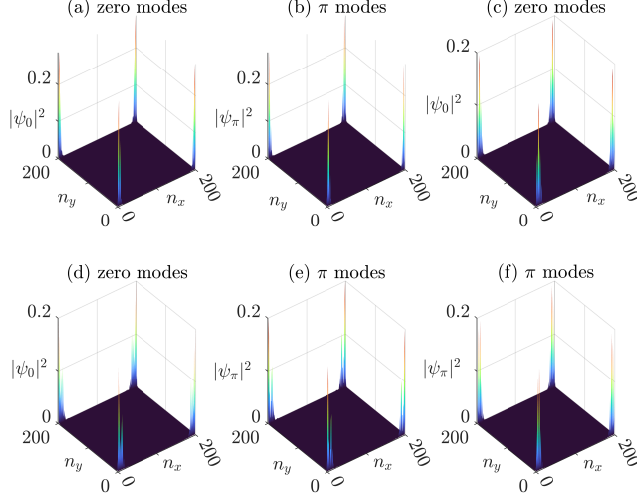


FIG. 5. Probability distributions of the corner modes of $U'(k_x, k_y)$ at critical points under OBCs. (a) shows the four Floquet states at $\mathcal{E} = 0$ in Fig. 4(c). (b) shows the four Floquet states at $\mathcal{E} = \pi$ in Fig. 4(c). (c) and (d) show the eight Floquet states at $\mathcal{E} = 0$ in Fig. 4(d). (e) and (f) show the eight Floquet states at $\mathcal{E} = \pi$ in Fig. 4(d).

are four (eight) zero modes and four (eight) π modes in Fig. 4(c) (Fig. 4(d)), whose IPRs are clearly larger than other states close to their quasienergies. Moreover, the numbers of zero and π Floquet corner modes at the critical points of $U'(k_x, k_y)$ are correctly counted by the invariants (ω_0, ω_π) according to Eq. (44), which verifies the rule of bulk-corner correspondence we proposed for 2D, chiral-symmetric driven systems.

To further illustrate the spatial configurations of Floquet corner modes at topological phase boundaries, we show in Figs. 5(a)–5(b) and Figs. 5(c)–5(f) the probability distributions of the zero and π eigenmodes in Figs. 4(c) and 4(d), respectively. We find that these zero and π modes are indeed corner-localized, irrespective of the bulk-gap closing at zero and π quasienergies. These corner states could thus survive topological transitions between different Floquet SOTI phases, offering characteristic signatures of gapless higher-order topology at Floquet critical points. Their coexistence at zero and π quasienergies further implies that they have no static counterparts and are unique to nonequilibrium Floquet settings. In principle, we could obtain as many coexisting zero and π corner modes as we want at the critical points of the system describe by $U'(k_x, k_y)$ via tuning its parameters, i.e., J_{x1} . Therefore, Floquet driving offers a flexible tool for us to enrich the higher-order topology at topological transition points and induce higher-order gSPT phases that are intrinsically nonequilibrium.

V. SUMMARY

In this work, we revealed the nontrivial topology and corner modes at the critical points between different Floquet SOTPs. Focusing on 2D systems with chiral symmetry, we uncovered the conditions for degenerate Floquet corner modes to appear at zero and π quasienergies when the bulk states remain gapless. Moreover, we analytically characterized the transitions between different Floquet SOTPs with gapless bulk spectra. To resolve the issue of bulk-corner correspondence, we proposed a pair of generalized winding numbers under the PBC based on the Cauchy's argument principle, which could correctly count the numbers of zero and π corner modes in both gapped and gapless Floquet SOTPs so long as the chiral symmetry is preserved. Going beyond the minimal model, we demonstrated the possibility of having as many zero and π corner modes as possible to coexist with a fully gapless quasienergy bulk, which is enabled by long-range couplings induced via Floquet driving. Our work not only extended the study of higher-order topology and bulk-corner correspondence to the critical points of nonequilibrium systems, but also unveiled the richness of Floquet gapless topology beyond first-order topological phases.

In future studies, it would be important to systematically check the stability of higher-order Floquet topology at critical points against disorder and many-body interactions. Floquet gapless higher-order topology beyond two spatial dimensions and in other symmetry classes are also interesting research topics. Finally, the experimental detection of Floquet higher-order topological criticality in quantum simulators like cold atoms, photonic and acoustic systems merits further explorations.

ACKNOWLEDGMENTS

This work is supported by the National Natural Science Foundation of China (Grants No. 12275260 and No. 11905211), the Fundamental Research Funds for the Central Universities (Grant No. 202364008), and the Young Talents Project of Ocean University of China.

Appendix A: Edge and corner zero modes of static models

In this Appendix, we compute exact solutions of zero-energy eigenmodes in the 1D CL and SSH models. We show that they can be exponentially localized around system edges

only in the gapped topological phases. These zero-mode solutions will be further used to construct corner zero modes of the coupled 2D CL-SSH model, as discussed in the main text. Explicit conditions for these eigenmodes to be localized exponentially at corners will be given.

After Fourier transformation, the Bloch Hamiltonian $H_x(k_x)$ of CL in the main text can be expressed in real space as

$$\begin{aligned}
H_x = & J_{x0} \sum_m (\hat{u}_m^\dagger \hat{v}_m + \text{H.c.}) \\
& + \frac{J_{x1}}{2} \sum_m [(\hat{u}_m^\dagger \hat{v}_{m+1} + \hat{u}_{m+1}^\dagger \hat{v}_m) + \text{H.c.}] \\
& + \frac{J_{x1}}{2i} \sum_m [(\hat{u}_m^\dagger \hat{u}_{m+1} - \hat{v}_m^\dagger \hat{v}_{m+1}) - \text{H.c.}], \tag{A1}
\end{aligned}$$

where m is the unit-cell index along x -direction. \hat{u}_m^\dagger and \hat{v}_m^\dagger create a fermion in the sublattices u and v of the m th unit cell on the upper and lower legs of the ladder [see Fig. 1(a)], respectively. Consider a half-infinite ladder with $m = 1, 2, \dots, \infty$. A general solution of the eigenvalue equation $H_x|\psi\rangle = E|\psi\rangle$ can be expanded as $|\psi\rangle = \sum_m (\psi_{m,u} \hat{u}_m^\dagger + \psi_{m,v} \hat{v}_m^\dagger) |\emptyset\rangle$, where $|\emptyset\rangle$ denotes the vacuum state. If $|\psi\rangle$ is a zero-energy eigenstate of H_x , it must satisfy $H_x|\psi\rangle = 0$, yielding

$$\begin{aligned}
& J_{x0} \sum_m (\psi_{m,v} \hat{u}_m^\dagger + \psi_{m,u} \hat{v}_m^\dagger) \\
& + \frac{J_{x1}}{2} \sum_m (\psi_{m+1,v} \hat{u}_m^\dagger + \psi_{m,v} \hat{u}_{m+1}^\dagger + \psi_{m+1,u} \hat{v}_m^\dagger + \psi_{m,u} \hat{v}_{m+1}^\dagger) \\
& + \frac{J_{x1}}{2i} \sum_m (\psi_{m+1,u} \hat{u}_m^\dagger - \psi_{m,u} \hat{u}_{m+1}^\dagger - \psi_{m+1,v} \hat{v}_m^\dagger + \psi_{m,v} \hat{v}_{m+1}^\dagger) = 0. \tag{A2}
\end{aligned}$$

Solving the difference equation for the coefficients $\psi_{m,u}$ and $\psi_{m,v}$, we find for any $m \in \mathbb{Z}^+$ that

$$\psi_{m,u} = i\psi_{m,v}, \quad \psi_{m,u} = \left(-\frac{J_{x0}}{J_{x1}}\right)^{m-1} \psi_{1,u}, \quad \psi_{m,v} = \left(-\frac{J_{x0}}{J_{x1}}\right)^{m-1} \psi_{1,v}. \tag{A3}$$

Therefore, up to a normalization constant, the wavefunction of zero-energy solution takes

the form

$$|\psi_L\rangle = \sum_{m=1}^{\infty} \left(-\frac{J_{x0}}{J_{x1}}\right)^{m-1} (\hat{u}_m^\dagger - i\hat{v}_m^\dagger)|\emptyset\rangle, \quad (\text{A4})$$

where ‘‘L’’ means left. It is clear that $|\psi_L\rangle$ represents an edge zero mode localized exponentially from site $m = 1$ if and only if $|J_{x1}| > |J_{x0}|$. At the critical point $|J_{x1}| = |J_{x0}|$, $|\psi_L\rangle$ becomes extended uniformly across all sites of the two legs. Another edge zero mode $|\psi_R\rangle$ (‘‘R’’ means right) can be found by considering the half-infinite chain with unit-cell indices $m = -\infty, \dots, M-1, M$ ($M \gg 1$) and solving $H_x|\psi_R\rangle = 0$, yielding

$$|\psi_R\rangle = \sum_{m=-\infty}^M \left(-\frac{J_{x0}}{J_{x1}}\right)^{M-m} (\hat{u}_m^\dagger + i\hat{v}_m^\dagger)|\emptyset\rangle. \quad (\text{A5})$$

The two modes $|\psi_L\rangle$ and $|\psi_R\rangle$ satisfy $\langle\psi_L|\psi_R\rangle = 0$, making them degenerate at $E = 0$.

Upon Fourier transformation, the Bloch Hamiltonian $H_y(k_y)$ of SSH model can be expressed in real space as

$$H_y = \sum_n \left(J_{y0} \hat{a}_n^\dagger \hat{b}_n + J_{y1} \hat{b}_n^\dagger \hat{a}_{n+1} + \text{H.c.} \right), \quad (\text{A6})$$

where n is the unit-cell index along y -direction. \hat{a}_n^\dagger and \hat{b}_n^\dagger creates a fermion on the sublattice a and b of the n th unit cell, respectively [see Fig. 1(a)]. Consider a half-infinite chain with $n = 1, 2, \dots, \infty$, a general solution of the eigenvalue equation $H_y|\psi'\rangle = E|\psi'\rangle$ can be expanded as $|\psi'\rangle = \sum_n (\varphi_{n,a} \hat{a}_n^\dagger + \varphi_{n,b} \hat{b}_n^\dagger)|\emptyset\rangle$, where $|\emptyset\rangle$ denotes the vacuum state. If $|\psi'\rangle$ is a zero-energy eigenstate of H_y , it must satisfy $H_y|\psi'\rangle = 0$, yielding

$$\sum_n \left(J_{y0} \varphi_{n,b} \hat{a}_n^\dagger + J_{y0} \varphi_{n,a} \hat{b}_n^\dagger + J_{y1} \varphi_{n+1,a} \hat{b}_n^\dagger + J_{y1} \varphi_{n,b} \hat{a}_{n+1}^\dagger \right) = 0. \quad (\text{A7})$$

Solving the difference equation for the coefficients $\varphi_{n,a}$ and $\varphi_{n,b}$, we find for any $n \in \mathbb{Z}^+$ that

$$\varphi_{n,a} = \left(-\frac{J_{y0}}{J_{y1}}\right)^{n-1} \varphi_{1,a}, \quad \varphi_{n,b} = 0. \quad (\text{A8})$$

Therefore, up to a normalization constant, the wavefunction of zero-energy solution takes the form

$$|\psi'_B\rangle = \sum_{n=1}^{\infty} \left(-\frac{J_{y0}}{J_{y1}}\right)^{n-1} \hat{a}_n^\dagger |\emptyset\rangle, \quad (\text{A9})$$

where “B” denotes bottom. It is clear that $|\psi'_B\rangle$ represents an edge zero mode localized exponentially along y -direction from the site $n = 1$ if and only if $|J_{y1}| > |J_{y0}|$. At the critical point $|J_{y1}| = |J_{y0}|$, $|\psi'_B\rangle$ becomes a charge density wave, which is extended uniformly across all the a sublattices of the system. Another edge zero mode $|\psi'_T\rangle$ (“T” denotes top) can be found by considering the half-infinite chain with unit-cell indices $n = -\infty, \dots, N - 1, N$ ($N \gg 1$) and solving $H_y|\psi'\rangle = 0$, yielding

$$|\psi'_T\rangle = \sum_{n=-\infty}^N \left(-\frac{J_{y0}}{J_{y1}}\right)^{N-n} \hat{b}_n^\dagger |\emptyset\rangle. \quad (\text{A10})$$

The two modes $|\psi'_B\rangle$ and $|\psi'_T\rangle$ satisfy $\langle\psi'_B|\psi'_T\rangle = 0$, affirming their degeneracy at $E = 0$. The conditions for them to be localized edge states are the same.

In two spatial dimensions, we can now construct four zero modes from the edge modes of 1D CL and SSH models. Their wave functions (up to normalization factors) are given by

$$|\Psi_{LB}\rangle = |\psi_L\rangle \otimes |\psi'_B\rangle, \quad |\Psi_{LT}\rangle = |\psi_L\rangle \otimes |\psi'_T\rangle, \quad (\text{A11})$$

$$|\Psi_{RB}\rangle = |\psi_R\rangle \otimes |\psi'_B\rangle, \quad |\Psi_{RT}\rangle = |\psi_R\rangle \otimes |\psi'_T\rangle. \quad (\text{A12})$$

When the conditions $|J_{x1}| > |J_{x0}|$ and $|J_{y1}| > |J_{y0}|$ are both satisfied, these four zero modes are exponentially localized at the left-bottom (LB), left-top (LT), right-bottom (RB) and right-top (RT) corners of the 2D lattice, respectively. These corner modes will all vanish in other parameter domains, including the critical regions where the bulk spectra are gapless. Their four-fold degeneracy is protected by the chiral symmetry of the 2D system.

Appendix B: Topology and bulk-edge correspondence of the kicked CL

In this Appendix, we establish the bulk-edge correspondence for the kicked CL from two complementary perspectives. Focusing on the edge, we obtain exact solutions at zero and π quasienergies for a half-infinite ladder, and reveal under what condition they could become exponentially localized edge modes. Focusing on the bulk, we generalize the definition of winding numbers following the strategy leading to Eq. (8) [73], and verify that our generalized winding numbers could correctly count the zero and π Floquet edge modes in both the gapped phases and at the critical points, thereby establishing bulk-edge correspondence

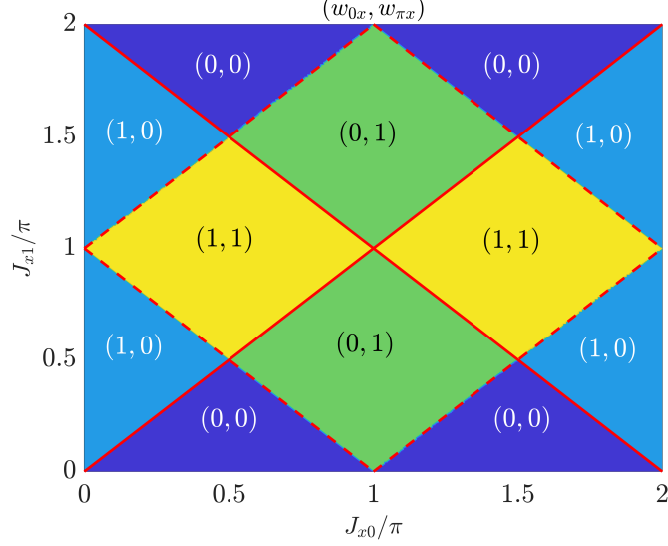


FIG. 6. Topological phase diagram of the 1D kicked CL. Each region with a uniform color corresponds to a gapped Floquet phase, with the winding numbers $(w_{0x}, w_{\pi x})$ denoted therein. The solid and dashed lines are given by Eq. (32), along which the bulk quasienergy gaps of $U_x(k_x)$ close at $E = 0$ and $E = \pm\pi$, respectively.

throughout the parameter space of the system. These two perspectives yield consistent results.

As a start, we obtain the topological phase diagram of $U_x(k_x)$ [Eq. (29)] for its gapped phases by evaluating the more conventional winding numbers in Eq. (37). We can expand the Floquet operator $U_{\alpha x}(k_x)$ [Eqs. (33) and (34)] in symmetric time frame α as

$$U_{\alpha x}(k_x) = \cos[\varepsilon(k_x)] - i(d_{x\alpha}\sigma_x + d_{z\alpha}\sigma_z), \quad \alpha = 1, 2. \quad (\text{B1})$$

The expression of $\varepsilon(k_x)$ has been given by Eq. (31). The components in front of Pauli matrices σ_x and σ_z are

$$d_{x1} = \sin J_{x0} \cos^2 \frac{J_{x1}}{2} \cos(\lambda' k_x) + \cos J_{x0} \sin J_{x1} \cos(\lambda k_x) - \sin J_{x0} \sin^2 \frac{J_{x1}}{2} \cos[(2\lambda - \lambda')k_x], \quad (\text{B2})$$

$$d_{z1} = \sin J_{x0} \cos^2 \frac{J_{x1}}{2} \sin(\lambda' k_x) + \cos J_{x0} \sin J_{x1} \sin(\lambda k_x) - \sin J_{x0} \sin^2 \frac{J_{x1}}{2} \sin[(2\lambda - \lambda')k_x], \quad (\text{B3})$$

$$d_{x2} = \sin J_{x1} \cos^2 \frac{J_{x0}}{2} \cos(\lambda k_x) + \cos J_{x1} \sin J_{x0} \cos(\lambda' k_x) - \sin J_{x1} \sin^2 \frac{J_{x0}}{2} \cos[(2\lambda' - \lambda)k_x], \quad (\text{B4})$$

$$d_{z2} = \sin J_{x1} \cos^2 \frac{J_{x0}}{2} \sin(\lambda k_x) + \cos J_{x1} \sin J_{x0} \sin(\lambda' k_x) - \sin J_{x1} \sin^2 \frac{J_{x0}}{2} \sin[(2\lambda' - \lambda)k_x], \quad (\text{B5})$$

where $\lambda = 1$ and $\lambda' = 0$. Plugging these expressions into Eq. (36) gives us the winding numbers (w_{1x}, w_{2x}) , whose combinations further yield the topological invariants $(w_{0x}, w_{\pi x})$ of $U_x(k_x)$ through Eq. (37). In Fig. 6, we report the numerical results of $(w_{0x}, w_{\pi x})$ in the parameter space $(J_{x0}, J_{x1}) \in [0, 2\pi] \times [0, 2\pi]$ of the kicked CL. As the $U_x(k_x)$ is invariant under the change of J_{x0} or J_{x1} by 2π , the phase diagrams in other parameter regions can be obtained by translating Fig. 6 along the J_{x0} and J_{x1} axes by integer multiples of 2π . Moreover, we notice that the lower-left quarter of Fig. 6, with $(J_{x0}, J_{x1}) \in [0, \pi] \times [0, \pi]$, already contains all possible topological phases of the system. Other parts of the phase diagram in Fig. 6 can be obtained by reflecting this lower-left quarter along the parameter axes $J_{x0} = \pi$ and $J_{x1} = \pi$. We can thus focus on characterizing the topological phases and transitions in the quarter of Fig. 6 with $(J_{x0}, J_{x1}) \in [0, \pi] \times [0, \pi]$ in the following discussions of this Appendix. General conclusions working for all parameter regions of the kicked CL will be summarized in Appendix D.

Next, we propose a generalization of the topological winding numbers $(w_{0x}, w_{\pi x})$ based on the Cauchy's argument principle [13], which is expected to be applicable in both the gapped and gapless regions [73]. In Eq. (B1), we may identify the Floquet effective Hamiltonian in the symmetric time frame α as $H_{\alpha x}(k_x) = [U_{\alpha x}^\dagger(k_x) - U_{\alpha x}(k_x)]/(2i)$, i.e.,

$$H_{\alpha x}(k_x) = d_{x\alpha} \sigma_x + d_{z\alpha} \sigma_z, \quad \alpha = 1, 2. \quad (\text{B6})$$

As $[H_{\alpha x}(k_x), U_{\alpha x}(k_x)] = 0$, the effective Hamiltonian $H_{\alpha x}(k_x)$ shares the same eigenstates and symmetries with the original Floquet operator $U_{\alpha x}(k_x)$. Meanwhile, when the Floquet bands of $U_{\alpha x}(k_x)$ touch at the quasienergy zero or π , the spectrum of $H_{\alpha x}(k_x)$ becomes gapless at $\varepsilon = 0$. Therefore, the critical points of $U_{\alpha x}(k_x)$ are the same as its effective Hamiltonian $H_{\alpha x}(k_x)$ in the J_{x0} - J_{x1} parameter space, even though they appear at different (quasi)energies.

With Eqs. (B1)–(B5) and following Ref. [13], we find the complex mapping functions of

effective Hamiltonians $H_{1x}(k_x)$ and $H_{2x}(k_x)$ as

$$\begin{aligned} f_{1x}(z) &= \sin J_{x0} \cos^2 \frac{J_{x1}}{2} + \cos J_{x0} \sin J_{x1} z - \sin J_{x0} \sin^2 \frac{J_{x1}}{2} z^2, \\ f_{2x}(z) &= \frac{(\sin J_{x1} \cos^2 \frac{J_{x0}}{2} z^2 + \cos J_{x1} \sin J_{x0} z - \sin J_{x1} \sin^2 \frac{J_{x0}}{2}) z}{z^2}. \end{aligned} \quad (\text{B7})$$

The Cauchy's argument principle then states that for $f_{\alpha x}(z)$, the difference between the number of its zeros ($N_{\alpha z}$) and poles ($N_{\alpha p}$) (including their multiplicities and orders) inside the unit circle $|z| = 1$ is an integer-quantized winding number, which will be denoted by $\omega_{\alpha x}$ ($\alpha = 1, 2$). However, this zero-pole counting rule needs to be slightly modified along the critical lines where the gaps close at quasienergy π [73]. Using $(\omega_{1x}, \omega_{2x})$, we can finally arrive at a pair of generalized topological invariants as

$$(\omega_{0x}, \omega_{\pi x}) = \frac{1}{2}(\omega_{1x} + \omega_{2x}, \omega_{1x} - \omega_{2x}). \quad (\text{B8})$$

We now verify that the invariants $(\omega_{0x}, \omega_{\pi x})$ in Eq. (B8) could reproduce the topological phase diagram in Fig. 6, i.e., we have $(\omega_{0x}, \omega_{\pi x}) = (w_{0x}, w_{\pi x})$ in all the gapped phases. Since the winding numbers could not change when the spectrum gap remains open, we can just do the zero-pole counting at one representative point within each gapped parameter region in order to characterize the corresponding gapped phase. Without losing generality, we can consider the representative points $(J_{x0}, J_{x1}) = (\pi/2, 0)$, $(0, \pi/2)$, $(\pi, \pi/2)$ and $(\pi/2, \pi)$ on the lower-left quarter of Fig. 6. The zero-pole counting for the $f_{1x}(z)$ and $f_{2x}(z)$ in Eq. (B7) can then be performed directly. For example, at $(J_{x0}, J_{x1}) = (\pi/2, \pi)$, we have $f_{1x}(z) = z^2$ and $f_{2x}(z) = -1$, yielding $N_{1z} - N_{1p} = \omega_{1x} = 2$ and $N_{2z} - N_{2p} = \omega_{2x} = 0$. From Eq. (B8), we then obtain $(\omega_{0x}, \omega_{\pi x}) = (1, 1)$, which are exactly identical to the winding numbers $(w_{0x}, w_{\pi x})$ shown in Fig. 6. One can repeat the calculations at other representative points. The final results confirm that for all the gapped phases, we have $(\omega_{0x}, \omega_{\pi x}) = (w_{0x}, w_{\pi x})$. The generalized winding numbers $(\omega_{0x}, \omega_{\pi x})$ thus predict the same phase diagram as $(w_{0x}, w_{\pi x})$ for gapped topological phases of the kicked CL.

Along the critical lines, the conventional winding numbers $(w_{0x}, w_{\pi x})$ can take half-integer values and may become ill-defined in general. Due to the Cauchy's argument principle, the generalized winding numbers $(\omega_{0x}, \omega_{\pi x})$ are still expected to be integers. To see this, we first consider the critical line $J_{x1} = J_{x0}$ within the lower-left quarter of Fig. 6 [i.e., with $J_{x0} \in$

$(0, \pi]$. There is a multi-critical point $J_{x1} = J_{x0} = \pi/2$ along this critical line, which divides it into two segments. Within the segment $J_{x0} \in (0, \pi/2)$ or $J_{x0} \in (\pi/2, \pi)$, the gap structure of the system remains unchanged, and we can pick up one representative point in each segment to analyze the generalized winding numbers $(\omega_{0x}, \omega_{\pi x})$. At $(J_{x0}, J_{x1}) = (\pi/3, \pi/3)$, we find $\omega_{1x} \equiv N_{1z} - N_{1p} = 0$ and $\omega_{2x} \equiv N_{2z} - N_{2p} = 0$, yielding $(\omega_{0x}, \omega_{\pi x}) = (0, 0)$ due to Eq. (B8), which remains valid along $J_{x1} = J_{x0}$ for $J_{x0} \in (0, \pi/2)$. At $(J_{x0}, J_{x1}) = (2\pi/3, 2\pi/3)$, we find $\omega_{1x} \equiv N_{1z} - N_{1p} = 1$ and $\omega_{2x} \equiv N_{2z} - N_{2p} = -1$, yielding $(\omega_{0x}, \omega_{\pi x}) = (0, 1)$ due to Eq. (B8), which remains valid along $J_{x1} = J_{x0}$ for $J_{x0} \in (\pi/2, \pi)$. Notably, we realize that the two segments $J_{x0} \in (0, \pi/2)$ and $J_{x0} \in (\pi/2, \pi)$ along the the critical line $J_{x1} = J_{x0}$ are topologically discriminated by the generalized winding number $\omega_{\pi x}$. Next, we consider the critical line $J_{x1} = \pi - J_{x0}$ within the lower-left quarter of Fig. 6, along which the quasienergy gap closes at $\pm\pi$ and a refined zero-pole counting rule is needed [73]. Specially, at the representative point $(J_{x0}, J_{x1}) = (\pi/3, 2\pi/3)$, we find $\omega_{1x} \equiv N_{1z} - N_{1p}/2 = 1$ and $\omega_{2x} \equiv N_{2z} - N_{2p}/2 = 1$, yielding $(\omega_{0x}, \omega_{\pi x}) = (1, 0)$ due to Eq. (B8), which remains valid along $J_{x1} = \pi - J_{x0}$ for $J_{x0} \in (0, \pi/2)$. At another representative point $(J_{x0}, J_{x1}) = (2\pi/3, \pi/3)$, we find $\omega_{1x} \equiv N_{1z} - N_{1p}/2 = 0$ and $\omega_{2x} \equiv N_{2z} - N_{2p}/2 = 0$, yielding $(\omega_{0x}, \omega_{\pi x}) = (0, 0)$ due to Eq. (B8), which remains valid along $J_{x1} = \pi - J_{x0}$ for $J_{x0} \in (\pi/2, \pi)$. We see that the two segments $J_{x0} \in (0, \pi/2)$ and $J_{x0} \in (\pi/2, \pi)$ along the the critical line $J_{x1} = \pi - J_{x0}$ are also topologically inequivalent, with the generalized winding number ω_{0x} taking different values. Finally, at the multi-critical point $(J_{x0}, J_{x1}) = (\pi/2, \pi/2)$, the spectral gaps close at both zero and π quasienergies. We find $\omega_{1x} \equiv N_{1z} - N_{1p}/2 = 0$ and $\omega_{2x} \equiv N_{2z} - N_{2p}/2 = 0$, yielding $(\omega_{0x}, \omega_{\pi x}) = (0, 0)$ due to Eq. (B8).

To sum up, we propose the following definitions for the generalized winding numbers $(\omega_{1x}, \omega_{2x})$ in two symmetric time frames

$$\omega_{\alpha x} = \begin{cases} N_{\alpha z} - N_{\alpha p}, & \Delta_{\pi} \neq 0, \\ N_{\alpha z} - N_{\alpha p}/2, & \Delta_{\pi} = 0, \end{cases} \quad \alpha = 1, 2, \quad (\text{B9})$$

where Δ_{π} measures the quasi-spectral gap of $U_x(k_x)$ at quasienergy π . Following this definition, the invariants $(\omega_{0x}, \omega_{\pi x})$ in Eq. (B8) are always integer quantized, as demonstrated in the above discussions. Moreover, they could completely characterize the bulk-edge correspondence of the kicked CL. This point will be confirmed below from the perspective of

edge states.

To simplify the calculation of edge states, we first make a basis transformation on the Floquet operator $U_x = \sum_{k_x} \hat{\Psi}_{k_x}^\dagger U_x(k_x) \hat{\Psi}_{k_x}$ of the kicked CL, where $U_x(k_x)$ is given by Eq. (29) and $\hat{\Psi}_{k_x}^\dagger \equiv (\hat{u}_{k_x}^\dagger, \hat{v}_{k_x}^\dagger)$, with $\hat{u}_{k_x}^\dagger$ ($\hat{v}_{k_x}^\dagger$) creating a fermion of quasimomentum k_x in the sublattice u (v) pertaining to the upper (lower) leg [see Fig. 1(a)]. Applying the unitary rotation $R = e^{i\frac{\pi}{4}\sigma_x}$, we obtain

$$\begin{aligned} \tilde{U}_x(k_x) &= RU_x(k_x)R^\dagger \\ &= e^{-iJ_{x0}\sigma_x} e^{-iJ_{x1}[\cos(k_x)\sigma_x + \sin(k_x)\sigma_y]}, \end{aligned} \quad (\text{B10})$$

together with the transformed basis

$$\hat{\Phi}_{k_x} \equiv \begin{pmatrix} \hat{a}_{k_x} \\ \hat{b}_{k_x} \end{pmatrix} = R \begin{pmatrix} \hat{u}_{k_x} \\ \hat{v}_{k_x} \end{pmatrix} = \frac{\sqrt{2}}{2} \begin{pmatrix} \hat{u}_{k_x} + i\hat{v}_{k_x} \\ i\hat{u}_{k_x} + \hat{v}_{k_x} \end{pmatrix}. \quad (\text{B11})$$

In this new basis, the Floquet operator is given by $U_x = \sum_{k_x} \hat{\Phi}_{k_x}^\dagger \tilde{U}_x(k_x) \hat{\Phi}_{k_x}$, and in the lattice representation it takes the form

$$U_x = e^{-iJ_{x0}\mathcal{H}_{x0}} e^{-iJ_{x1}\mathcal{H}_{x1}}, \quad (\text{B12})$$

where

$$\begin{aligned} \mathcal{H}_{x0} &\equiv \sum_m (\hat{a}_m^\dagger \hat{b}_m + \text{H.c.}), \\ \mathcal{H}_{x1} &\equiv \sum_m (\hat{b}_m^\dagger \hat{a}_{m+1} + \text{H.c.}). \end{aligned} \quad (\text{B13})$$

The \hat{a}_m^\dagger and \hat{b}_m^\dagger are Fourier transformations of $\hat{a}_{k_x}^\dagger$ and $\hat{b}_{k_x}^\dagger$. To proceed, we solve the Heisenberg equations for \hat{a}_m^\dagger and \hat{b}_m^\dagger under the time-evolution governed by \mathcal{H}_{x0} and \mathcal{H}_{x1} . For a

half-infinite ladder with the unit cell index m going from 1 to $+\infty$, the solutions are

$$\begin{aligned}
e^{it\mathcal{H}_{x0}}\hat{a}_m^\dagger e^{-it\mathcal{H}_{x0}} &= \cos(t)\hat{a}_m^\dagger + i\sin(t)\hat{b}_m^\dagger, \\
e^{it\mathcal{H}_{x0}}\hat{b}_m^\dagger e^{-it\mathcal{H}_{x0}} &= \cos(t)\hat{b}_m^\dagger + i\sin(t)\hat{a}_m^\dagger, \\
e^{it\mathcal{H}_{x1}}\hat{a}_m^\dagger e^{-it\mathcal{H}_{x1}} &= \begin{cases} \hat{a}_m^\dagger, & m = 1, \\ \cos(t)\hat{a}_m^\dagger + i\sin(t)\hat{b}_{m-1}^\dagger, & m > 1, \end{cases} \\
e^{it\mathcal{H}_{x1}}\hat{b}_m^\dagger e^{-it\mathcal{H}_{x1}} &= \cos(t)\hat{b}_m^\dagger + i\sin(t)\hat{a}_{m+1}^\dagger.
\end{aligned} \tag{B14}$$

Using these solutions, we could further obtain

$$U_x^\dagger \hat{a}_m^\dagger U_x = \begin{cases} \cos(J_{x0})\hat{a}_m^\dagger + i\sin(J_{x0})[\cos(J_{x1})\hat{b}_m^\dagger + i\sin(J_{x1})\hat{a}_{m+1}^\dagger], & m = 1, \\ \cos(J_{x0})[\cos(J_{x1})\hat{a}_m^\dagger + i\sin(J_{x1})\hat{b}_{m-1}^\dagger] + i\sin(J_{x0})[\cos(J_{x1})\hat{b}_m^\dagger + i\sin(J_{x1})\hat{a}_{m+1}^\dagger], & m > 1, \end{cases} \tag{B15}$$

$$U_x^\dagger \hat{b}_m^\dagger U_x = \begin{cases} \cos(J_{x0})[\cos(J_{x1})\hat{b}_m^\dagger + i\sin(J_{x1})\hat{a}_{m+1}^\dagger] + i\sin(J_{x0})\hat{a}_m^\dagger, & m = 1, \\ \cos(J_{x0})[\cos(J_{x1})\hat{b}_m^\dagger + i\sin(J_{x1})\hat{a}_{m+1}^\dagger] + i\sin(J_{x0})[\cos(J_{x1})\hat{a}_m^\dagger + i\sin(J_{x1})\hat{b}_{m-1}^\dagger], & m > 1, \end{cases} \tag{B16}$$

Let us denote $|\psi_L^{(0)}\rangle \equiv \hat{\psi}_0^\dagger|\emptyset\rangle$ and $|\psi_L^{(\pi)}\rangle \equiv \hat{\psi}_\pi^\dagger|\emptyset\rangle$ (“L” means left) as the eigenstates of U_x with quasienergies 0 and π , where $|\emptyset\rangle$ represents the vacuum state. These zero and π eigenmodes should satisfy

$$U_x^\dagger \hat{\psi}_0^\dagger U_x = \hat{\psi}_0^\dagger, \quad U_x^\dagger \hat{\psi}_\pi^\dagger U_x = -\hat{\psi}_\pi^\dagger. \tag{B17}$$

To proceed, we expand $|\psi_L^{(0)}\rangle$ and $|\psi_L^{(\pi)}\rangle$ in the transformed basis $(\hat{a}_m^\dagger, \hat{b}_m^\dagger)$ as

$$\hat{\psi}_0^\dagger = \sum_{m=1}^{\infty} (A_m \hat{a}_m^\dagger + B_m \hat{b}_m^\dagger), \tag{B18}$$

$$\hat{\psi}_\pi^\dagger = \sum_{m=1}^{\infty} (C_m \hat{a}_m^\dagger + D_m \hat{b}_m^\dagger). \tag{B19}$$

Inserting these expansions into Eq. (B17) and solving the difference equations for the coef-

ficients A_m , B_m , C_m and D_m , we find that (up to normalization constants):

$$\hat{\psi}_0^\dagger = \sum_{m=1}^{\infty} \left[-\frac{\tan(J_{x0}/2)}{\tan(J_{x1}/2)} \right]^{m-1} \left[\cos\left(\frac{J_{x0}}{2}\right) \hat{a}_m^\dagger - i \sin\left(\frac{J_{x0}}{2}\right) \hat{b}_m^\dagger \right], \quad (\text{B20})$$

$$\hat{\psi}_\pi^\dagger = \sum_{m=1}^{\infty} \left[\frac{1}{\tan(J_{x0}/2) \tan(J_{x1}/2)} \right]^{m-1} \left[\sin\left(\frac{J_{x0}}{2}\right) \hat{a}_m^\dagger + i \cos\left(\frac{J_{x0}}{2}\right) \hat{b}_m^\dagger \right]. \quad (\text{B21})$$

Transforming back to the original basis $(\hat{u}_m^\dagger, \hat{v}_m^\dagger)$ with $\hat{a}_m^\dagger = \frac{\sqrt{2}}{2}(\hat{u}_m^\dagger - i\hat{v}_m^\dagger)$ and $\hat{b}_m^\dagger = \frac{\sqrt{2}}{2}(-i\hat{u}_m^\dagger + \hat{v}_m^\dagger)$, we finally obtain the zero and π eigenmodes of the kicked CL as

$$|\psi_L^{(0)}\rangle = \sum_{m=1}^{\infty} \left[-\frac{\tan(J_{x0}/2)}{\tan(J_{x1}/2)} \right]^{m-1} (\rho_m \hat{u}_m^\dagger - i\lambda_m \hat{v}_m^\dagger) |\emptyset\rangle, \quad (\text{B22})$$

$$|\psi_L^{(\pi)}\rangle = \sum_{m=1}^{\infty} \left[\frac{1}{\tan(J_{x0}/2) \tan(J_{x1}/2)} \right]^{m-1} (\lambda_m \hat{u}_m^\dagger + i\rho_m \hat{v}_m^\dagger) |\emptyset\rangle, \quad (\text{B23})$$

where $\rho_m \equiv \frac{\sqrt{2}}{2} [\cos(\frac{J_{x0}}{2}) - \sin(\frac{J_{x0}}{2})]$ and $\lambda_m \equiv \frac{\sqrt{2}}{2} [\cos(\frac{J_{x0}}{2}) + \sin(\frac{J_{x0}}{2})]$. Both the zero and π modes should come in pairs due to the degeneracy enforced by chiral symmetry. The rest of zero and π eigenmodes can be obtained by considering the half-infinite ladder with unit-cell indices $m = -\infty, \dots, M-1, M$ ($M \gg 1$), yielding

$$|\psi_R^{(0)}\rangle = \sum_{m=-\infty}^M \left[-\frac{\tan(J_{x0}/2)}{\tan(J_{x1}/2)} \right]^{M-m} (\lambda_m \hat{u}_m^\dagger + i\rho_m \hat{v}_m^\dagger) |\emptyset\rangle, \quad (\text{B24})$$

$$|\psi_R^{(\pi)}\rangle = \sum_{m=-\infty}^M \left[\frac{1}{\tan(J_{x0}/2) \tan(J_{x1}/2)} \right]^{M-m} (\rho_m \hat{u}_m^\dagger - i\lambda_m \hat{v}_m^\dagger) |\emptyset\rangle, \quad (\text{B25})$$

where ‘‘R’’ means right. Since ρ_m and λ_m could not vanish together, the global profiles of these zero and π modes are solely determined by their prefactors $\tan(J_{x0}/2)/\tan(J_{x1}/2)$ and $1/[\tan(J_{x0}/2) \tan(J_{x1}/2)]$.

We now analyze the conditions for these eigenmodes to be edge-localized. The zero mode in Eq. (B22) is exponentially localized around the left edge ($m = 1$) if and only if $|\tan(J_{x1}/2)| > |\tan(J_{x0}/2)|$. In the phase diagram Fig. 6, this condition is satisfied in the regions with $J_{x1} \in (J_{x0}, 2\pi - J_{x0})$ for $J_{x0} \in (0, \pi)$ and with $J_{x1} \in (2\pi - J_{x0}, J_{x0})$ for $J_{x0} \in (\pi, 2\pi)$. The π mode in Eq. (B23) is exponentially localized around the left edge ($m = 1$) if and only if $|\tan(J_{x0}/2) \tan(J_{x1}/2)| > 1$. In the phase diagram Fig. 6, this condition is fulfilled in the regions with $J_{x1} \in (\pi - J_{x0}, \pi + J_{x0})$ for $J_{x0} \in (0, \pi)$ and with

$J_{x1} \in (J_{x0} - \pi, 3\pi - J_{x0})$ for $J_{x0} \in (\pi, 2\pi)$. Referring to the winding numbers $(w_{0x}, w_{\pi x})$ in Fig. 6, their relationship with the generalized invariants $(\omega_{0x}, \omega_{\pi x})$ analyzed below Eq. (B8), and the chiral-symmetry-enforced twofold degeneracy of zero and π eigenmodes, we end up with the bulk-edge correspondence for the kicked CL as

$$(N_{0x}, N_{\pi x}) = 2(|w_{0x}|, |w_{\pi x}|) = 2(|\omega_{0x}|, |\omega_{\pi x}|), \quad (\text{B26})$$

where N_{0x} ($N_{\pi x}$) counts the number of exponentially localized edge modes at quasienergy zero (π). This relation holds true among the gapped phases of the kicked CL.

We next consider the bulk-edge correspondence at phase boundaries. Along the critical lines $J_{x1} = \pi \pm J_{x0}$ with $J_{x0} \in (0, \pi)$, $J_{x1} = -\pi + J_{x0}$ with $J_{x0} \in (\pi, 2\pi)$, and $J_{x1} = 3\pi - J_{x0}$ with $J_{x0} \in (\pi, 2\pi)$, our solution in Eq. (B22) permits the survival of one localized Floquet zero mode at each edge $[(N_{0x}, N_{\pi x}) = (2, 0)]$. The generalized winding numbers in Eq. (B8) take $(\omega_{0x}, \omega_{\pi x}) = (1, 0)$ along these phase boundaries, while the conventional winding numbers in Eq. (37) yield $(w_{0x}, w_{\pi x}) = (1, 1/2)$. Along the critical lines $J_{x1} = J_{x0}$ and $J_{x1} = 2\pi - J_{x0}$ with $J_{x0} \in (\pi/2, 3\pi/2)$, our solution in Eq. (B23) permits the survival of one localized Floquet π mode at each edge $[(N_{0x}, N_{\pi x}) = (0, 2)]$. The generalized winding numbers in Eq. (B8) take $(\omega_{0x}, \omega_{\pi x}) = (0, 1)$ along these phase boundaries, while the conventional winding numbers in Eq. (37) yield $(w_{0x}, w_{\pi x}) = (1/2, 1)$. Along the other critical lines in Fig. 6, the solutions in Eqs. (B22) and (B23) are no longer Floquet edge modes. The generalized winding numbers in Eq. (B8) take $(\omega_{0x}, \omega_{\pi x}) = (0, 0)$ along these phase boundaries, while at least one of the conventional winding numbers $(w_{0x}, w_{\pi x})$ in Eq. (37) takes a half-integer value.

Overall, we find that the generalized winding numbers $(\omega_{0x}, \omega_{\pi x})$ could always count the numbers of Floquet zero and π edge modes along the critical lines correctly, in the sense that $(N_{0x}, N_{\pi x}) = 2(|\omega_{0x}|, |\omega_{\pi x}|)$, whereas the conventional winding numbers $(w_{0x}, w_{\pi x})$ may become invalid due to the emergence of half-quantized values. Looking back at Eq. (B26), we finally conclude that Eq. (40) in the main text describes the most general bulk-edge correspondence of the kicked CL, working equally well in its gapped phases and along its phase boundaries where the bulk spectra become gapless. We expect the Eq. (40) to hold also in other 1D, two-band chiral-symmetric driven systems, regardless of the presence of a quasienergy gap.

Appendix C: Floquet zero and π corner modes of the periodically kicked CL-SSH model

In Appendices A and B, we have analytically obtained the zero-energy edge modes of the SSH model and the zero/ π -quasienergy edge modes of the periodically kicked CL. Since the Floquet operator of our 2D driven CL-SSH model is given by

$$U = U_x \otimes U_y, \quad (\text{C1})$$

with $U_x = e^{-iJ_{x0}\mathcal{H}_{x0}}e^{-iJ_{x1}\mathcal{H}_{x1}}$ [Eq. (B12)] and $U_y = e^{-iH_y}$ [Eq. (A6)], the corner-localized solutions of U at zero and π quasienergies can be deduced from the edge modes of U_x and U_y under OBCs.

First, we notice that any Floquet eigenstate of U must be in the direct product form $|\Psi\rangle = |\psi\rangle \otimes |\psi'\rangle$ with quasienergy $\mathcal{E} = \varepsilon + \varepsilon' \bmod 2\pi$, where $|\psi\rangle$ ($|\psi'\rangle$) is an eigenstate of U_x (U_y) with quasienergy ε (ε'). Second, for the $|\Psi\rangle$ to be a corner-localized eigenmode, neither $|\psi\rangle$ nor $|\psi'\rangle$ should be an extended bulk state. Otherwise, $|\Psi\rangle$ would be extended along at least one spatial dimension. Therefore, $|\Psi\rangle = |\psi\rangle \otimes |\psi'\rangle$ is corner-localized if and only if both $|\psi\rangle$ and $|\psi'\rangle$ are localized eigenstates of their corresponding propagators U_x and U_y under OBCs. Third, the edge-state solutions of U_y are also those of H_y [Eq. (A6)], whose quasienergy must be zero [Eqs. (A9) and (A10)]. Meanwhile, the edge-state solutions of U_x [Eq. (B12)] have quasienergy zero [Eqs. (B22) and (B24)] or π [Eqs. (B23) and (B25)]. Therefore, the corner-localized solutions of $U = U_x \otimes U_y$ could only appear at the quasienergy $\mathcal{E} = 0$ or $\mathcal{E} = \pm\pi$.

With these considerations, we can write down all the possibly corner-localized eigenmodes of U under the OBCs as

$$|\Psi_{\text{LB}}^{(\mathcal{E})}\rangle = |\psi_{\text{L}}^{(\mathcal{E})}\rangle \otimes |\psi'_{\text{B}}\rangle, \quad |\Psi_{\text{LT}}^{(\mathcal{E})}\rangle = |\psi_{\text{L}}^{(\mathcal{E})}\rangle \otimes |\psi'_{\text{T}}\rangle, \quad (\text{C2})$$

$$|\Psi_{\text{RB}}^{(\mathcal{E})}\rangle = |\psi_{\text{R}}^{(\mathcal{E})}\rangle \otimes |\psi'_{\text{B}}\rangle, \quad |\Psi_{\text{RT}}^{(\mathcal{E})}\rangle = |\psi_{\text{R}}^{(\mathcal{E})}\rangle \otimes |\psi'_{\text{T}}\rangle, \quad (\text{C3})$$

where $\mathcal{E} = 0$ and π . Explicit expressions of $|\psi_{\text{L,R}}^{(0)}\rangle$, $|\psi_{\text{L,R}}^{(\pi)}\rangle$ and $|\psi'_{\text{B,T}}\rangle$ are given by Eqs. (B22)–(B24), (B23)–(B25) and (A9)–(A10), respectively. It is clear that once these eigenstates appear as corner modes with the quasienergy \mathcal{E} (0 or π), they must be fourfold degenerate.

From the wave functions in Eqs. (C2) and (C3), we can further identify the conditions for these states to be corner-localized, as detailed below.

(i) $|\psi_{L,R}^{(0)}\rangle$ are edge-localized zero modes if and only if $|\tan(J_{x1}/2)| > |\tan(J_{x0}/2)|$ [Eqs. (B22) and (B24)].

(ii) $|\psi_{L,R}^{(\pi)}\rangle$ are edge-localized π modes if and only if $|\tan(J_{x0}/2)\tan(J_{x1}/2)| > 1$ [Eqs. (B23) and (B25)].

(iii) $|\psi'_{B,T}\rangle$ are edge-localized zero modes if and only if $|J_{y1}| > |J_{y0}|$ [Eqs. (A9) and (A10)].

(iv) Referring to (i) and (iii), the states $|\Psi_{LB}^{(0)}\rangle$, $|\Psi_{LT}^{(0)}\rangle$, $|\Psi_{RB}^{(0)}\rangle$ and $|\Psi_{RT}^{(0)}\rangle$ constitute four corner-localized Floquet eigenmodes with quasienergy $\mathcal{E} = 0$ if and only if

$$|\tan(J_{x1}/2)| > |\tan(J_{x0}/2)| \quad \& \quad |J_{y1}| > |J_{y0}|. \quad (\text{C4})$$

(v) Referring to (ii) and (iii), the states $|\Psi_{LB}^{(\pi)}\rangle$, $|\Psi_{LT}^{(\pi)}\rangle$, $|\Psi_{RB}^{(\pi)}\rangle$ and $|\Psi_{RT}^{(\pi)}\rangle$ constitute four corner-localized Floquet eigenmodes with quasienergy $\mathcal{E} = \pi$ if and only if

$$|\tan(J_{x0}/2)\tan(J_{x1}/2)| > 1 \quad \& \quad |J_{y1}| > |J_{y0}|. \quad (\text{C5})$$

(vi) There will be four Floquet corner modes at $\mathcal{E} = 0$ and four other corner modes at $\mathcal{E} = \pi$ if and only if the conditions in Eqs. (C4) and (C5) are both satisfied.

(vii) When none of the conditions in Eqs. (C4) and (C5) are fulfilled, the system will have no Floquet corner modes.

These analytical results are well consistent with our numerical calculations, especially along phase boundaries between different HOTPs as reported in the main text.

Appendix D: Bulk-corner correspondence of the periodically kicked CL-SSH model

In this Appendix, we propose the topological invariants that could count the numbers of zero and π Floquet corner modes in each parameter region, thereby establishing the rule of bulk-corner correspondence for our kicked CL-SSH model. Importantly, this rule allows us to know along which phase boundary the zero or π Floquet corner modes could survive topological phase transitions, making the associated critical points topologically nontrivial. It also applies to the Floquet HOTPs in other 2D systems with chiral symmetry and under similar driving protocols (i.e., only system parameters along one of the two spatial dimensions

depend on driving fields).

In the main text, we have introduced the generalized winding number ω_y [Eq. (16)] and established the bulk-edge correspondence [Eq. (17)] for the static SSH model. The Eq. (16) can also describe the topological phases and bulk-edge correspondence of the one-period free-evolution operator $U_y = e^{-iH_y}$ of the SSH model [with the H_y given by Eq. (A6)]. On the other hand, the bulk-edge correspondence of the kicked CL has been captured by the generalized winding numbers $(\omega_{0x}, \omega_{\pi x})$ in Eq. (B26). Since the zero and π Floquet corner modes of the driven CL-SSH model [Eq. (24)] can only be formed via coupling edge states of its parent systems, we can directly infer the bulk-corner correspondence for the periodically kicked CL-SSH model, i.e.,

$$(N_0, N_\pi) = 4(|\omega_{0x}\omega_y|, |\omega_{\pi x}\omega_y|) \equiv 4(\omega_0, \omega_\pi). \quad (\text{D1})$$

The invariants (ω_0, ω_π) , as defined in Eq. (D1), could characterize the higher-order topology and bulk-corner correspondence of all the gapped and gapless phases in our kicked CL-SSH model.

We can verify Eq. (D1) as follows. First, due to the Eq. (17), we only need to prove the following relations for the kicked CL-SSH model

$$(N_0, N_\pi) = \begin{cases} (0, 0), & |J_{y1}| \leq |J_{y0}|, \\ 4(|\omega_{0x}|, |\omega_{\pi x}|), & |J_{y1}| > |J_{y0}|. \end{cases} \quad (\text{D2})$$

According to Eqs. (C4) and (C5), we will have no zero or π Floquet corner modes when $|J_{y1}| \leq |J_{y0}|$, i.e., $(N_0, N_\pi) = (0, 0)$. The first equality in Eq. (D2) is thus confirmed. Under the condition $|J_{y1}| > |J_{y0}|$, we can further analyze the values of ω_{0x} and $\omega_{\pi x}$ following the Appendix B and Eq. (32).

To proceed, we factorize the complex-continued functions in Eq. (B7) as follows

$$\begin{aligned} f_{1x}(z) &= -\sin J_{x0} \sin^2 \frac{J_{x1}}{2} \left(z + \frac{\tan \frac{J_{x0}}{2}}{\tan \frac{J_{x1}}{2}} \right) \left(z - \frac{1}{\tan \frac{J_{x0}}{2} \tan \frac{J_{x1}}{2}} \right), \\ f_{2x}(z) &= \frac{\sin J_{x1} \cos^2 \frac{J_{x0}}{2} \left(z + \frac{\tan \frac{J_{x0}}{2}}{\tan \frac{J_{x1}}{2}} \right) \left(z - \tan \frac{J_{x0}}{2} \tan \frac{J_{x1}}{2} \right) z}{z^2}. \end{aligned} \quad (\text{D3})$$

The function $f_{1x}(z)$ has no poles. Referring to Eq. (B9), we should have

$$\omega_{1x} = \begin{cases} 2, & |\tan \frac{J_{x1}}{2}| > |\tan \frac{J_{x0}}{2}| & \& \quad |\tan \frac{J_{x0}}{2} \tan \frac{J_{x1}}{2}| > 1, \\ 1, & |\tan \frac{J_{x1}}{2}| > |\tan \frac{J_{x0}}{2}| & \& \quad |\tan \frac{J_{x0}}{2} \tan \frac{J_{x1}}{2}| \leq 1, \\ 1, & |\tan \frac{J_{x1}}{2}| \leq |\tan \frac{J_{x0}}{2}| & \& \quad |\tan \frac{J_{x0}}{2} \tan \frac{J_{x1}}{2}| > 1, \\ 0, & |\tan \frac{J_{x1}}{2}| \leq |\tan \frac{J_{x0}}{2}| & \& \quad |\tan \frac{J_{x0}}{2} \tan \frac{J_{x1}}{2}| \leq 1. \end{cases} \quad (\text{D4})$$

Next, referring to the Eq. (32), it is straightforward to verify that the conditions $J_{x0} \pm J_{x1} = (2\nu + 1)\pi$ and $|\tan \frac{J_{x0}}{2} \tan \frac{J_{x1}}{2}| \neq 1$ cannot be simultaneously fulfilled. Therefore, we can use $\omega_{2x} = N_{2z} - N_{2p}$ to find the ω_{2x} from $f_{2x}(z)$ when $|\tan \frac{J_{x0}}{2} \tan \frac{J_{x1}}{2}| \neq 1$, yielding

$$\omega_{2x} = \begin{cases} 0, & |\tan \frac{J_{x1}}{2}| > |\tan \frac{J_{x0}}{2}| & \& \quad |\tan \frac{J_{x0}}{2} \tan \frac{J_{x1}}{2}| > 1, \\ 1, & |\tan \frac{J_{x1}}{2}| > |\tan \frac{J_{x0}}{2}| & \& \quad |\tan \frac{J_{x0}}{2} \tan \frac{J_{x1}}{2}| < 1, \\ -1, & |\tan \frac{J_{x1}}{2}| \leq |\tan \frac{J_{x0}}{2}| & \& \quad |\tan \frac{J_{x0}}{2} \tan \frac{J_{x1}}{2}| > 1, \\ 0, & |\tan \frac{J_{x1}}{2}| \leq |\tan \frac{J_{x0}}{2}| & \& \quad |\tan \frac{J_{x0}}{2} \tan \frac{J_{x1}}{2}| < 1. \end{cases} \quad (\text{D5})$$

When $J_{x0} \pm J_{x1} = (2\nu + 1)\pi$, we have $\Delta_\pi = 0$ and $|\tan \frac{J_{x0}}{2} \tan \frac{J_{x1}}{2}| = 1$. According to Eq. (B9), we should use $\omega_{2x} = N_{2z} - N_{2p}/2$ to compute the ω_{2x} from $f_{2x}(z)$ in this case, yielding $\omega_{2x} = 1$ for $|\tan \frac{J_{x1}}{2}| > |\tan \frac{J_{x0}}{2}|$ and $\omega_{2x} = 0$ for $|\tan \frac{J_{x1}}{2}| \leq |\tan \frac{J_{x0}}{2}|$. These results can be combined into the second and fourth lines of Eq. (D5), leaving us with

$$\omega_{2x} = \begin{cases} 0, & |\tan \frac{J_{x1}}{2}| > |\tan \frac{J_{x0}}{2}| & \& \quad |\tan \frac{J_{x0}}{2} \tan \frac{J_{x1}}{2}| > 1, \\ 1, & |\tan \frac{J_{x1}}{2}| > |\tan \frac{J_{x0}}{2}| & \& \quad |\tan \frac{J_{x0}}{2} \tan \frac{J_{x1}}{2}| \leq 1, \\ -1, & |\tan \frac{J_{x1}}{2}| \leq |\tan \frac{J_{x0}}{2}| & \& \quad |\tan \frac{J_{x0}}{2} \tan \frac{J_{x1}}{2}| > 1, \\ 0, & |\tan \frac{J_{x1}}{2}| \leq |\tan \frac{J_{x0}}{2}| & \& \quad |\tan \frac{J_{x0}}{2} \tan \frac{J_{x1}}{2}| \leq 1. \end{cases} \quad (\text{D6})$$

Plugging Eqs. (D4) and (D6) into the definition of generalized winding numbers $(\omega_{0x}, \omega_{\pi x})$

in Eq. (D6) finally yields

$$(\omega_{0x}, \omega_{\pi x}) = \begin{cases} (1, 1), & |\tan \frac{J_{x1}}{2}| > |\tan \frac{J_{x0}}{2}| & \& \quad |\tan \frac{J_{x0}}{2} \tan \frac{J_{x1}}{2}| > 1, \\ (1, 0), & |\tan \frac{J_{x1}}{2}| > |\tan \frac{J_{x0}}{2}| & \& \quad |\tan \frac{J_{x0}}{2} \tan \frac{J_{x1}}{2}| \leq 1, \\ (0, 1), & |\tan \frac{J_{x1}}{2}| \leq |\tan \frac{J_{x0}}{2}| & \& \quad |\tan \frac{J_{x0}}{2} \tan \frac{J_{x1}}{2}| > 1, \\ (0, 0), & |\tan \frac{J_{x1}}{2}| \leq |\tan \frac{J_{x0}}{2}| & \& \quad |\tan \frac{J_{x0}}{2} \tan \frac{J_{x1}}{2}| \leq 1. \end{cases} \quad (\text{D7})$$

If the rule of bulk-corner correspondence in Eq. (D1) is true, we should have the following results for our kicked CL-SSH model according to Eqs. (D2) and (D7), i.e.,

$$(N_0, N_\pi) = \begin{cases} (4, 4), & |J_{y1}| > |J_{y0}| & \& \quad |\tan \frac{J_{x1}}{2}| > |\tan \frac{J_{x0}}{2}| & \& \quad |\tan \frac{J_{x0}}{2} \tan \frac{J_{x1}}{2}| > 1, \\ (4, 0), & |J_{y1}| > |J_{y0}| & \& \quad |\tan \frac{J_{x1}}{2}| > |\tan \frac{J_{x0}}{2}| & \& \quad |\tan \frac{J_{x0}}{2} \tan \frac{J_{x1}}{2}| \leq 1, \\ (0, 4), & |J_{y1}| > |J_{y0}| & \& \quad |\tan \frac{J_{x1}}{2}| \leq |\tan \frac{J_{x0}}{2}| & \& \quad |\tan \frac{J_{x0}}{2} \tan \frac{J_{x1}}{2}| > 1, \\ (0, 0), & \text{Otherwise.} \end{cases} \quad (\text{D8})$$

These relations are perfectly consistent with our counting of zero and π Floquet corner modes N_0 and N_π following the points (i)–(vii) of Appendix C, which are nevertheless deduced from exact solutions of corner states. Our proposed rule of bulk-corner correspondence in Eq. (D1) is then verified.

-
- [1] D. Xiao, M.-C. Chang, and Q. Niu, Berry phase effects on electronic properties, *Rev. Mod. Phys.* **82**, 1959 (2010).
 - [2] M. Z. Hasan and C. L. Kane, *Colloquium: Topological insulators*, *Rev. Mod. Phys.* **82**, 3045 (2010).
 - [3] X.-L. Qi and S.-C. Zhang, Topological insulators and superconductors, *Rev. Mod. Phys.* **83**, 1057 (2011).
 - [4] C.-K. Chiu, J. C. Y. Teo, A. P. Schnyder, and S. Ryu, Classification of topological quantum matter with symmetries, *Rev. Mod. Phys.* **88**, 035005 (2016).
 - [5] X.-G. Wen, *Colloquium: Zoo of quantum-topological phases of matter*, *Rev. Mod. Phys.* **89**, 041004 (2017).

- [6] X.-G. Wen, Choreographed entanglement dances: Topological states of quantum matter, *Science* **363**, eaal3099 (2019).
- [7] J. McGreevy, Generalized Symmetries in Condensed Matter, *Annu. Rev. Condens. Matter Phys.* **14**, 57 (2023).
- [8] C. Fang, H. Weng, X. Dai, and Z. Fang, Topological nodal line semimetals, *Chin. Phys. B* **25**, 117106 (2016).
- [9] A. A. Burkov, Weyl Metals, *Annu. Rev. Condens. Matter Phys.* **9**, 359 (2018).
- [10] N. P. Armitage, E. J. Mele, and A. Vishwanath, Weyl and Dirac semimetals in three-dimensional solids, *Rev. Mod. Phys.* **90**, 015001 (2018).
- [11] B. Q. Lv, T. Qian, and H. Ding, Experimental perspective on three-dimensional topological semimetals, *Rev. Mod. Phys.* **93**, 025002 (2021).
- [12] R. Verresen, R. Moessner, and F. Pollmann, One-dimensional symmetry protected topological phases and their transitions, *Phys. Rev. B* **96**, 165124 (2017).
- [13] R. Verresen, N. G. Jones, and F. Pollmann, Topology and Edge Modes in Quantum Critical Chains, *Phys. Rev. Lett.* **120**, 057001 (2018).
- [14] N. G. Jones and R. Verresen, Asymptotic Correlations in Gapped and Critical Topological Phases of 1D Quantum Systems, *J. Stat. Phys.* **175**, 1164 (2019).
- [15] T.-K. Ng, Edge states in antiferromagnetic quantum spin chains, *Phys. Rev. B* **50**, 555 (1994).
- [16] M. Cheng and H.-H. Tu, Majorana edge states in interacting two-chain ladders of fermions, *Phys. Rev. B* **84**, 094503 (2011).
- [17] L. Fidkowski, R. M. Lutchyn, C. Nayak, and M. P. A. Fisher, Majorana zero modes in one-dimensional quantum wires without long-ranged superconducting order, *Phys. Rev. B* **84**, 195436 (2011).
- [18] J. P. Kestner, B. Wang, J. D. Sau, and S. Das Sarma, Prediction of a gapless topological Haldane liquid phase in a one-dimensional cold polar molecular lattice, *Phys. Rev. B* **83**, 174409 (2011).
- [19] A. Keselman and E. Berg, Gapless symmetry-protected topological phase of fermions in one dimension, *Phys. Rev. B* **91**, 235309 (2015).
- [20] F. Iemini, L. Mazza, D. Rossini, R. Fazio, and S. Diehl, Localized Majorana-Like Modes in a Number-Conserving Setting: An Exactly Solvable Model, *Phys. Rev. Lett.* **115**, 156402 (2015).

- [21] N. Lang and H. P. Büchler, Topological states in a microscopic model of interacting fermions, *Phys. Rev. B* **92**, 041118 (2015).
- [22] J. Ruhman and E. Altman, Topological degeneracy and pairing in a one-dimensional gas of spinless fermions, *Phys. Rev. B* **96**, 085133 (2017).
- [23] T. Scaffidi, D. E. Parker, and R. Vasseur, Gapless Symmetry-Protected Topological Order, *Phys. Rev. X* **7**, 041048 (2017).
- [24] W. Berdanier, M. Kolodrubetz, S. A. Parameswaran, and R. Vasseur, Floquet quantum criticality, *PNAS* **115**, 9491 (2018).
- [25] D. E. Parker, T. Scaffidi, and R. Vasseur, Topological Luttinger liquids from decorated domain walls, *Phys. Rev. B* **97**, 165114 (2018).
- [26] H.-C. Jiang, Z.-X. Li, A. Seidel, and D.-H. Lee, Symmetry protected topological Luttinger liquids and the phase transition between them, *Sci. Bull.* **63**, 753 (2018).
- [27] A. Keselman, E. Berg, and P. Azaria, From one-dimensional charge conserving superconductors to the gapless Haldane phase, *Phys. Rev. B* **98**, 214501 (2018).
- [28] D. Yates, Y. Lemonik, and A. Mitra, Central Charge of Periodically Driven Critical Kitaev Chains, *Phys. Rev. Lett.* **121**, 076802 (2018).
- [29] R. Verresen, Topology and edge states survive quantum criticality between topological insulators, arXiv:2003.05453.
- [30] C. M. Duque, H.-Y. Hu, Y.-Z. You, V. Khemani, R. Verresen, and R. Vasseur, Topological and symmetry-enriched random quantum critical points, *Phys. Rev. B* **103**, L100207 (2021).
- [31] R. Thorngren, A. Vishwanath, and R. Verresen, Intrinsically gapless topological phases, *Phys. Rev. B* **104**, 075132 (2021).
- [32] R. Verresen, R. Thorngren, N. G. Jones, and F. Pollmann, Gapless topological phases and symmetry-enriched quantum criticality, *Phys. Rev. X* **11**, 041059 (2021).
- [33] R. R. Kumar, Y. R. Kartik, S. Rahul, and S. Sarkar, Multi-critical topological transition at quantum criticality, *Sci. Rep.* **11**, 1004 (2021).
- [34] U. Borla, R. Verresen, J. Shah, and S. Moroz, Gauging the Kitaev chain, *SciPost Phys.* **10**, 148 (2021).
- [35] X.-J. Yu, R.-Z. Huang, H.-H. Song, L. Xu, C. Ding, and L. Zhang, Conformal Boundary Conditions of Symmetry-Enriched Quantum Critical Spin Chains, *Phys. Rev. Lett.* **129**, 210601 (2022).

- [36] A. Cerjan and T. A. Loring, Local invariants identify topology in metals and gapless systems, *Phys. Rev. B* **106**, 064109 (2022).
- [37] A. J. Friedman, B. Ware, R. Vasseur, and A. C. Potter, Topological edge modes without symmetry in quasiperiodically driven spin chains, *Phys. Rev. B* **105**, 115117 (2022).
- [38] N. G. Jones, R. Thorngren, and R. Verresen, Bulk-Boundary Correspondence and Singularity-Filling in Long-Range Free-Fermion Chains, *Phys. Rev. Lett.* **130**, 246601 (2023).
- [39] R. Wen and A. C. Potter, Bulk-boundary correspondence for intrinsically gapless symmetry-protected topological phases from group cohomology, *Phys. Rev. B* **107**, 245127 (2023).
- [40] R. Wen and A. C. Potter, Bulk-boundary correspondence for intrinsically gapless symmetry-protected topological phases from group cohomology, *Phys. Rev. B* **107**, 245127 (2023).
- [41] L. Li, M. Oshikawa, and Y. Zheng, Intrinsically/Purely Gapless-SPT from Non-Invertible Duality Transformations, arXiv:2307.04788.
- [42] S.-J. Huang and M. Cheng, Topological holography, quantum criticality, and boundary states, arXiv:2310.16878.
- [43] R. Wen and A. C. Potter, Classification of 1+1D gapless symmetry protected phases via topological holography, arXiv:2311.00050.
- [44] S. Prembabu, R. Thorngren, and R. Verresen, Boundary-deconfined quantum criticality at transitions between symmetry-protected topological chains, *Phys. Rev. B* **109**, L201112 (2024).
- [45] L. Li, M. Oshikawa, and Y. Zheng, Decorated defect construction of gapless-SPT states, *SciPost Phys.* **17**, 013 (2024).
- [46] X.-J. Yu, S. Yang, H.-Q. Lin, and S.-K. Jian, Universal Entanglement Spectrum in One-Dimensional Gapless Symmetry Protected Topological States, *Phys. Rev. Lett.* **133**, 026601 (2024).
- [47] X.-J. Yu and W.-L. Li, Fidelity susceptibility at the Lifshitz transition between the noninteracting topologically distinct quantum critical points, *Phys. Rev. B* **110**, 045119 (2024).
- [48] W.-H. Zhong, W.-L. Li, Y.-C. Chen, and X.-J. Yu, Topological edge modes and phase transitions in a critical fermionic chain with long-range interactions, *Phys. Rev. A* **110**, 022212 (2024).
- [49] H.-L. Zhang, H.-Z. Li, S. Yang, and X.-J. Yu, Quantum phase transition and critical behavior between the gapless topological phases, *Phys. Rev. A* **109**, 062226 (2024).

- [50] L. Su and M. Zeng, Gapless symmetry-protected topological phases and generalized deconfined critical points from gauging a finite subgroup, *Phys. Rev. B* **109**, 245108 (2024).
- [51] X. Wen, Exactly solvable non-unitary time evolution in quantum critical systems I: effect of complex spacetime metrics, *J. Stat. Mech.* **2024**, 103103 (2024).
- [52] S.-J. Huang, Fermionic quantum criticality through the lens of topological holography, arXiv:2405.09611.
- [53] T. Ando, S. Ryu, and M. Watanabe, Gauge theory and mixed state criticality, arXiv:2411.04360.
- [54] J. Fang, Q. Zhou, and X. Wen, Phase Transitions in Quasi-Periodically Driven Quantum Critical Systems: Analytical Results, arXiv:2501.04795.
- [55] X.-J. Yu, S. Yang, S. Liu, H.-Q. Lin, and S.-K. Jian, Gapless Symmetry-Protected Topological States in Measurement-Only Circuits, arXiv:2501.03851.
- [56] Z. Tan, K. Wang, S. Yang, F. Shen, F. Jin, X. Zhu, Y. Ji, S. Xu, J. Chen, Y. Wu, C. Zhang, Y. Gao, N. Wang, Y. Zou, A. Zhang, T. Li, Z. Bao, Z. Zhu, J. Zhong, Z. Cui, Y. Han, Y. He, H. Wang, J. Yang, Y. Wang, J. Shen, G. Liu, Z. Song, J. Deng, H. Dong, P. Zhang, S.-K. Jian, H. Li, Z. Wang, Q. Guo, C. Song, X.-J. Yu, H. Wang, H.-Q. Lin, F. Wu, Exploring nontrivial topology at quantum criticality in a superconducting processor, arXiv:2501.04679.
- [57] T. Oka and H. Aoki, Photovoltaic Hall effect in graphene, *Phys. Rev. B* **79**, 081406(R) (2009).
- [58] D. Y. H. Ho and J. Gong, Quantized Adiabatic Transport In Momentum Space, *Phys. Rev. Lett.* **109**, 010601 (2012).
- [59] Q.-J. Tong, J.-H. An, J. Gong, H.-G. Luo, and C. H. Oh, Generating many Majorana modes via periodic driving: A superconductor model, *Phys. Rev. B* **87**, 201109(R) (2013).
- [60] L. Jiang, T. Kitagawa, J. Alicea, A. R. Akhmerov, D. Pekker, G. Refael, J. I. Cirac, E. Demler, M. D. Lukin, and P. Zoller, Majorana Fermions in Equilibrium and in Driven Cold-Atom Quantum Wires, *Phys. Rev. Lett.* **106**, 220402 (2011).
- [61] M. S. Rudner, N. H. Lindner, E. Berg, and M. Levin, Anomalous Edge States and the Bulk-Edge Correspondence for Periodically Driven Two-Dimensional Systems, *Phys. Rev. X* **3**, 031005 (2013).
- [62] L. Zhou, C. Chen, and J. Gong, Floquet semimetal with Floquet-band holonomy, *Phys. Rev. B* **94**, 075443 (2016).
- [63] J. Cayssol, B. Dóra, F. Simon, and R. Moessner, Floquet topological insulators, *Physica*

- Status Solidi RRL **7**, 101 (2013).
- [64] M. Bukov, L. D' Alessio, and A. Polkovnikov, Universal high-frequency behavior of periodically driven systems: from dynamical stabilization to Floquet engineering, *Adv. Phys.* **64**, 139 (2015).
- [65] A. Eckardt, *Colloquium: Atomic quantum gases in periodically driven optical lattices*, *Rev. Mod. Phys.* **89**, 011004 (2017).
- [66] T. Oka and S. Kitamura, Floquet engineering of quantum materials, *Annu. Rev. Condens. Matter Phys.* **10**, 387 (2019).
- [67] M. S. Rudner and N. H. Lindner, Band structure engineering and non-equilibrium dynamics in Floquet topological insulators, *Nat. Rev. Phys.* **2**, 229 (2020).
- [68] F. Harper, R. Roy, M. S. Rudner, and S. L. Sondhi, Topology and broken symmetry in floquet systems, *Annu. Rev. Condens. Matter Phys.* **11**, 345 (2020).
- [69] S. Bandyopadhyay, S. Bhattacharjee and D. Sen, Driven quantum many-body systems and out-of-equilibrium topology, *J. Phys.: Condens. Matter* **33**, 393001 (2021).
- [70] A. de la Torre, D. M. Kennes, M. Claassen, S. Gerber, J. W. McIver, and M. A. Sentef, *Colloquium: Nonthermal pathways to ultrafast control in quantum materials*, *Rev. Mod. Phys.* **93**, 041002 (2021).
- [71] L. Zhou and D.-J. Zhang, Non-Hermitian floquet topological matter—A review, *Entropy* **25**, 1401 (2023).
- [72] F. Zhan, R. Chen, Z. Ning, D.-S. Ma, Z. Wang, D.-H. Xu, and R. Wang, Perspective: Floquet engineering topological states from effective models towards realistic materials, *Quantum Front.* **3**, 21 (2024).
- [73] L. Zhou, J. Gong, and X.-J. Yu, Topological edge states at Floquet quantum criticality, [arXiv:2410.15395](https://arxiv.org/abs/2410.15395).
- [74] G. Cardoso, H.-C. Yeh, L. Korneev, A. G. Abanov, A. Mitra, Gapless Floquet topology, [arXiv:2411.02526](https://arxiv.org/abs/2411.02526).
- [75] L. Trifunovic and P. W. Brouwer, Higher-Order Topological Band Structures, *Phys. Status Solidi B* **258**, 2000090 (2021).
- [76] B. Xie, H.-X. Wang, X. Zhang, P. Zhan, J.-H. Jiang, M. Lu, and Y. Chen, Higher-order band topology, *Nat. Rev. Phys.* **3**, 520 (2021).
- [77] A. K. Ghosh, T. Nag, and A. Saha, Generation of higher-order topological insulators using

- periodic driving, *J. Phys.: Condens. Matter* **36**, 093001 (2024).
- [78] Y.-B. Yang, J.-H. Wang, K. Li, and Y. Xu, Higher-order topological phases in crystalline and non-crystalline systems: a review, *J. Phys.: Condens. Matter* **36**, 283002 (2024).
- [79] M. Sitte, A. Rosch, E. Altman, and L. Fritz, Topological Insulators in Magnetic Fields: Quantum Hall Effect and Edge Channels with a Nonquantized θ Term, *Phys. Rev. Lett.* **108**, 126807 (2012).
- [80] F. Zhang, C. L. Kane, and E. J. Mele, Surface State Magnetization and Chiral Edge States on Topological Insulators, *Phys. Rev. Lett.* **110**, 046404 (2013).
- [81] R.-J. Slager, L. Rademaker, J. Zaanen, and L. Balents, Impurity-bound states and Green's function zeros as local signatures of topology, *Phys. Rev. B* **92**, 085126 (2015).
- [82] W. A. Benalcazar, B. A. Bernevig, and T. L. Hughes, Quantized electric multipole insulators, *Science* **357**, 61-66 (2017).
- [83] W. A. Benalcazar, B. A. Bernevig, and T. L. Hughes, Electric multipole moments, topological multipole moment pumping, and chiral hinge states in crystalline insulators, *Phys. Rev. B* **96**, 245115 (2017).
- [84] J. Langbehn, Y. Peng, L. Trifunovic, F. von Oppen, and P. W. Brouwer, Reflection-symmetric second-order topological insulators and superconductors, *Phys. Rev. Lett.* **119**, 246401 (2017).
- [85] Z. Song, Z. Fang, and C. Fang, $(d-2)$ -Dimensional edge states of rotation symmetry protected topological states, *Phys. Rev. Lett.* **119**, 246402 (2017).
- [86] F. Schindler, A. M. Cook, M. G. Vergniory, Z. Wang, S. S. P. Parkin, B. A. Bernevig, and T. Neupert, Higher-order topological insulators, *Sci. Adv.* **4**, eaat0346 (2018).
- [87] M. Geier, L. Trifunovic, M. Hoskam, and P. W. Brouwer, Second-order topological insulators and superconductors with an order-two crystalline symmetry, *Phys. Rev. B* **97**, 205135 (2018).
- [88] R. W. Bomantara, L. Zhou, J. Pan, and J. Gong, Coupled-wire construction of static and Floquet second-order topological insulators, *Phys. Rev. B* **99**, 045441 (2019).
- [89] R. Seshadri, A. Dutta, and D. Sen, Generating a second-order topological insulator with multiple corner states by periodic driving, *Phys. Rev. B* **100**, 115403 (2019).
- [90] Y. Peng and G. Refael, Floquet Second-Order Topological Insulators from Nonsymmorphic Space-Time Symmetries, *Phys. Rev. Lett.* **123**, 016806 (2019).
- [91] M. Rodriguez-Vega, A. Kumar, and B. Seradjeh, Higher-order Floquet topological phases with corner and bulk bound states, *Phys. Rev. B* **100**, 085138 (2019).

- [92] T. Nag, V. Juričić, and B. Roy, Out of equilibrium higher-order topological insulator: Floquet engineering and quench dynamics, *Phys. Rev. Research* **1**, 032045(R) (2019).
- [93] B. Huang, and W. V. Liu, Floquet Higher-Order Topological Insulators with Anomalous Dynamical Polarization, *Phys. Rev. Lett.* **124**, 216601 (2020).
- [94] H. Hu, B. Huang, E. Zhao, and W. V. Liu, Dynamical Singularities of Floquet Higher-Order Topological Insulators, *Phys. Rev. Lett.* **124**, 057001 (2020).
- [95] J. Pan and L. Zhou, Non-Hermitian Floquet second order topological insulators in periodically quenched lattices, *Phys. Rev. B* **102**, 094305 (2020).
- [96] A. K. Ghosh, G. C. Paul, and A. Saha, Higher order topological insulator via periodic driving, *Phys. Rev. B* **101**, 235403 (2020).
- [97] Y. Meng, G. Chen, and S. Jia, Second-order topological insulator in a coinless discrete-time quantum walk, *Phys. Rev. A* **102**, 012203 (2020).
- [98] W. Zhu, Y. D. Chong, and J. Gong, Floquet higher-order topological insulator in a periodically driven bipartite lattice, *Phys. Rev. B* **103**, L041402 (2021).
- [99] R. V. Bhat and S. Bera, Out of equilibrium chiral higher order topological insulator on a π -flux square lattice, *J. Phys.: Condens. Matter* **33**, 164005 (2021).
- [100] S. Franca, F. Hassler, and I. C. Fulga, Simulating Floquet topological phases in static systems, *SciPost Phys. Core* **4**, 007 (2021).
- [101] R.-X. Zhang and Z.-C. Yang, Tunable fragile topology in Floquet systems, *Phys. Rev. B* **103**, L121115 (2021).
- [102] W. Zhu, Y. D. Chong, and J. Gong, Symmetry analysis of anomalous Floquet topological phases, *Phys. Rev. B* **104**, L020302 (2021).
- [103] L. Zhou, Floquet Second-Order Topological Phases in Momentum Space, *Nanomaterials* **11**, 1170 (2021).
- [104] W. Zhu, H. Xue, J. Gong, Y. Chong, and B. Zhang, Time-periodic corner states from Floquet higher-order topology, *Nat. Commun.* **13**, 11 (2022).
- [105] J. Jin, L. He, J. Lu, E. J. Mele, and B. Zhen, Floquet Quadrupole Photonic Crystals Protected by Space-Time Symmetry, *Phys. Rev. Lett.* **129**, 063902 (2022).
- [106] S. Franca, F. Hassler, and I. C. Fulga, Topological reflection matrix, *Phys. Rev. B* **105**, 155121 (2022).
- [107] A. K. Ghosh, T. Nag, and A. Saha, Systematic generation of the cascade of anomalous

- dynamical first- and higher-order modes in Floquet topological insulators, *Phys. Rev. B* **105**, 115418 (2022).
- [108] Z. Ning, B. Fu, D.-H. Xu, and R. Wang, Tailoring quadrupole topological insulators with periodic driving and disorder, *Phys. Rev. B* **105**, L201114 (2022).
- [109] Y. Lei, X.-W. Luo, and S. Zhang, Second-order topological insulator in periodically driven optical lattices, *Opt. Express* **30**, 24048-24061 (2022).
- [110] L. Zhou, R. W. Bomantara, and S. Wu, q th-root non-Hermitian Floquet topological insulators, *SciPost Phys.* **13**, 015 (2022).
- [111] K. Plekhanov, M. Thakurathi, D. Loss, and J. Klinovaja, Floquet second-order topological superconductor driven via ferromagnetic resonance, *Phys. Rev. Research* **1**, 032013(R) (2019).
- [112] R. W. Bomantara and J. Gong, Measurement-only quantum computation with Floquet Majorana corner modes, *Phys. Rev. B* **101**, 085401 (2020).
- [113] R. W. Bomantara, Time-induced second-order topological superconductors, *Phys. Rev. Research* **2**, 033495 (2020).
- [114] Y. Peng, Floquet higher-order topological insulators and superconductors with space-time symmetries, *Phys. Rev. Research* **2**, 013124 (2020).
- [115] S. Chaudhary, A. Haim, Y. Peng, and G. Refael, Phonon-induced Floquet topological phases protected by space-time symmetries, *Phys. Rev. Research* **2**, 043431 (2020).
- [116] D. Vu, R.-X. Zhang, Z.-C. Yang, and S. D. Sarma, Superconductors with anomalous Floquet higher-order topology, *Phys. Rev. B* **104**, L140502 (2021).
- [117] A. K. Ghosh, T. Nag, and A. Saha, Floquet generation of a second-order topological superconductor, *Phys. Rev. B* **103**, 045424 (2021).
- [118] A. K. Ghosh, T. Nag, and A. Saha, Floquet second order topological superconductor based on unconventional pairing, *Phys. Rev. B* **103**, 085413 (2021).
- [119] A. K. Ghosh, T. Nag, and A. Saha, Dynamical construction of quadrupolar and octupolar topological superconductors, *Phys. Rev. B* **105**, 155406 (2022).
- [120] B. Huang, V. Novičenko, A. Eckardt, and G. Juzeliūnas, Floquet chiral hinge modes and their interplay with Weyl physics in a three-dimensional lattice, *Phys. Rev. B* **104**, 104312 (2021).
- [121] B.-Q. Wang, H. Wu, and J.-H. An, Engineering exotic second-order topological semimetals by periodic driving, *Phys. Rev. B* **104**, 205117 (2021).
- [122] W. Zhu, M. Umer, and J. Gong, Floquet higher-order Weyl and nexus semimetals, *Phys.*

- Rev. Research **3**, L032026 (2021).
- [123] S. Ghosh, K. Saha, and K. Sengupta, Hinge-mode dynamics of periodically driven higher-order Weyl semimetals, *Phys. Rev. B* **105**, 224312 (2022).
- [124] X.-L. Du, R. Chen, R. Wang, and D.-H. Xu, Weyl nodes with higher-order topology in an optically driven nodal-line semimetal, *Phys. Rev. B* **105**, L081102 (2022).
- [125] M. Creutz, End States, Ladder Compounds, and Domain-Wall Fermions, *Phys. Rev. Lett.* **83**, 2636 (1999).
- [126] W. P. Su, J. R. Schrieffer, and A. J. Heeger, Solitons in Polyacetylene, *Phys. Rev. Lett.* **42**, 1698 (1979).
- [127] S. Basu, *Quantum Hall Effect* (Cambridge University Press, Cambridge, UK, 2024).
- [128] L. Zhou and Q. Du, Floquet topological phases with fourfold-degenerate edge modes in a driven spin-1/2 Creutz ladder, *Phys. Rev. A* **101**, 033607 (2020).
- [129] J. K. Asboth and H. Obuse, Bulk-boundary correspondence for chiral symmetric quantum walks, *Phys. Rev. B* **88**, 121406(R) (2013).